VILNIUS UNIVERSITY
FACULTY OF CHEMISTRY AND GEOSCIENCES
INSTITUTE OF CHEMISTRY
DEPARTMENT OF ANALYTICAL AND ENVIRONMENTAL CHEMISTRY

Eglė Ežerskytė
Major study field Chemistry
Master thesis

SYNTHESIS, STRUCTURAL, AND OPTICAL CHARACTERISTICS OF GdPO$_4$:Ln^{3+} (Ln^{3+} = Ce^{3+}, Tb^{3+}, Eu^{3+}) NANOPARTICLES

Scientific adviser
prof. dr. Artūras Katelnikovas

Vilnius 2022

CONTENTS

ABBREVIATIONS

BET	Brunauer – Emmet – Teller
CIE	Commission Internationale de l'Eclairage
CN	Coordination Number
CT	Charge Transfer
ET	Energy Transfer
Gd-DTPA	Gadopentetic Acid/Gadopentetate Dimeglumine
ISO	International Organization for Standardization
Ln/Ln^{3+}	Lanthanide/Lanthanide(III) ion
MMCT	Metal to Metal Charge Transfer
MR	Magnetic Resonance
MRI	Magnetic Resonance Imaging
NIR	Near Infrared
NPs	Nanoparticles
NUV	Near Ultraviolet
OECD	Organization for Economic Cooperation and Development
PL	Photoluminescence
SEM	Scanning Electron Microscopy
XRD	X-ray Diffraction

INTRODUCTION

Inorganic luminescent nanoparticles doped with various lanthanide ions are greatly requested in such globally vital areas as energetics, biomedicine, anti-counterfeiting, etc. [1]. However, the synthesis of such materials usually requires ignoring the principles of green chemistry. Most synthesis routes for obtaining NPs of various phosphors (thermal decomposition, hot – injection, etc.) are dependent on environmentally hazardous precursors and solvents, which, in addition, lead to the formation of hydrophobic NPs, narrowing down their potential applicability range (e.g., biomedicine) [2].

In the context of this thesis, optically active NPs were obtained via a hydrothermal synthesis route that, in the case of this research, is considered to meet the fundamentals of green chemistry since no volatile or toxic materials are released to the environment during and after the synthesis process. Moreover, lanthanide ions doped $GdPO_4$ NPs, synthesized via the hydrothermal method, are hydrophilic, indicating that the solid form of these phosphors can be effortlessly redispersed in an aqueous media, which, in turn, heightens the odds of practical use of these materials in the biomedical field [3].

Furthermore, due to overlapping energy levels of specific lanthanide ions, inorganic phosphors containing Ce^{3+} and Tb^{3+} or Tb^{3+} and Eu^{3+} pairs stand out with the efficient energy transfer phenomenon enabling the excitation in the spectral range in which the lone species of lanthanide ions does not absorb the energy for its emission to occur. For instance, if the host lattice containing Tb^{3+} additionally adopts Ce^{3+}, the emission of Tb^{3+} increases by several folds, and the emission color of such phosphor might range from blue to green depending on the Ce^{3+}/Tb^{3+} ratio. Similarly, phosphors containing the Tb^{3+}/Eu^{3+} pair might emit radiation in the green-yellow-red range [4, 5]. Luminescent materials with the on-demand-controlled emission color are appealing as the anti-counterfeit pigments in documents, banknotes, valuable goods, etc.

This master thesis reports the synthesis, structural, and spectroscopic investigation of $GdPO_4$ NPs doped with Ce^{3+}, Tb^{3+}, or Eu^{3+} and their various combinations. This research aims to evaluate the applicability of synthesized phosphors as bioimaging or anti-counterfeit agents. The tasks of this work were formulated as follows:

1. optimization of hydrothermal synthesis parameters for the host matrix ($GdPO_4$) NPs;
2. structural and spectroscopic investigation of $GdPO_4$ NPs doped with Ce^{3+}, Tb^{3+}, or Eu^{3+};
3. structural and spectroscopic investigation of $GdPO_4$ NPs doped with Ce^{3+}/Tb^{3+}, and Tb^{3+}/Eu^{3+} pairs;
4. structural and spectroscopic investigation of $GdPO_4$ NPs doped with $Ce^{3+}/Tb^{3+}/Eu^{3+}$.

This master thesis is written in English (61 pages) and consists of the following elements: list of abbreviations, introduction, literature review, experimental section, results and discussion, conclusions, references (64), summaries in both English and Lithuanian, list of publications and conference attendance, supplementary material. This work contains 39 figures, two tables, and four appendixes with 31 tables.

1. LITERATURE OVERVIEW

1.1 Structural properties of rhabdophane (trigonal) phase of lanthanide orthophosphates

In nature, monazite (monoclinic) and xenotime (tetragonal) minerals of lanthanide orthophosphates are the most abundant, whereas crystals of churcite (monoclinic) and rhapdophane (trigonal) structure occur less frequently [6, 7].

The rhabdophane phase of $LnPO_4$ is mainly obtained via hydrothermal, aqueous coprecipitation, or microwave-assisted coprecipitation routes. Since wet chemical synthesis methods of the rhabdophane phase are superior (cheaper, less time-consuming, and more ecofriendly) than other synthesis methods, they have gained much scientific interest, especially in the field of luminescent materials [8].

Images of the crystal lattice (along different axes) of the trigonal phase (with space group $P3_121$) of lanthanide orthophosphate are presented in Figure 1 [9]. CN of each Ln ion in the rhabdophane phase is 8 since they are coordinated with 8 oxygen atoms forming LnO_8 polyhedrons. Each P(V) ion is coordinated with four oxygen atoms forming PO_4 tetrahedrons; thus, the CN of P(V) is 4. A single LnO_8 polyhedron shares four edges with other LnO_8 polyhedrons and two edges with PO_4 tetrahedrons. Such connection order of polyhedrons in the trigonal phase enables the formation of zeolitic channels along the c axis. These channels contain crystalline water that, in turn, affects the luminescent properties of $LnPO_4$ phosphors [10-12].
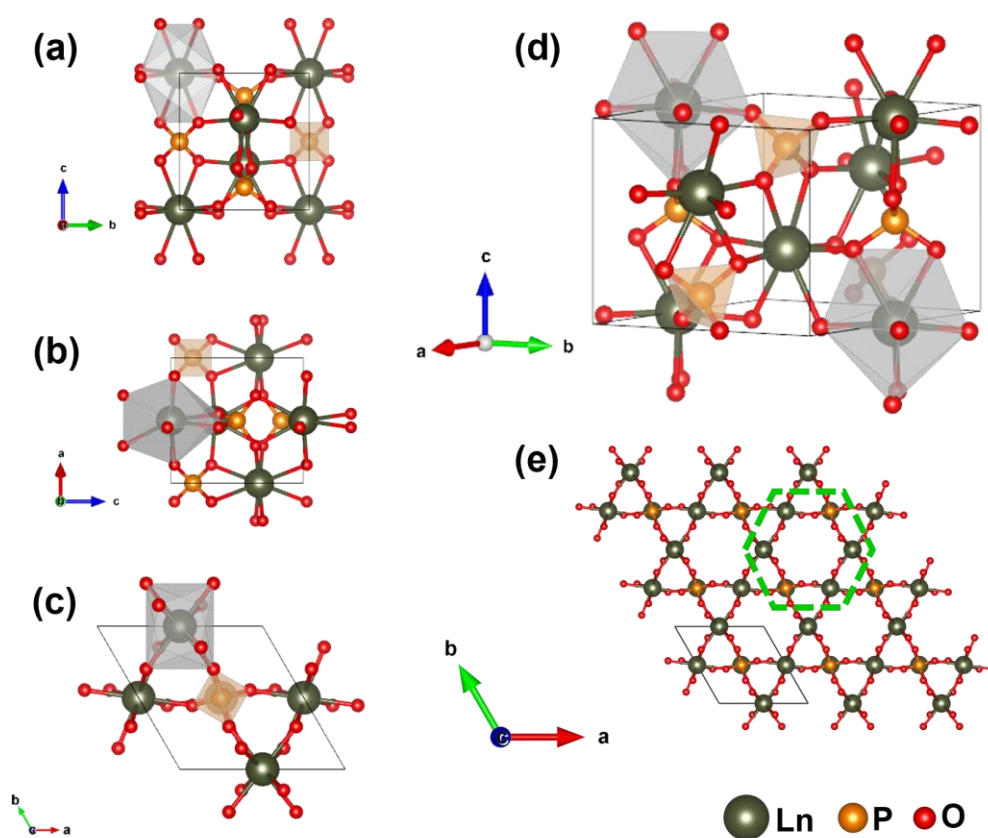

Figure 1. The trigonal (rhabdophane) $LnPO_4$ unit cell: along *a*-axis (a), along *b*-axis (b), along *c*-axis (c), and along standard orientation of crystal shape (d); fragment of the trigonal $LnPO_4$ crystal structure along *c*-axis with zeolitic channel highlighted in green dashed line (e).

Since this thesis focuses on GdPO$_4$ nanoparticles doped with single Ce^{3+}, Tb^{3+}, Eu^{3+}, and their combinations, the correlation between Ln^{3+} ionic radii and the trigonal LnPO$_4$ unit cell parameters should be discussed as well (Table 1). Unsurprisingly, with decreasing ionic radius in the order, Ce > Eu > Gd > Tb, all unit cell parameters slightly decrease, meaning that CePO$_4$ adopts the largest trigonal unit cell and TbPO$_4$ – the smallest.

Table 1. The correlation between Ln^{3+} ionic radii and the trigonal LnPO$_4$ unit cell parameters [13, 14].

Ln	The ionic radius of Ln^{3+}, Å	Unit cell parameters of the hexagonal LnPO$_4$		
		a, Å	b, Å	c, Å
Ce	1.143	6.78	7.01	6.45
Eu	1.066	6.65	6.84	6.33
Gd	1.053	6.64	6.83	6.32
Tb	1.040	6.60	6.82	6.31

1.2 Hydrothermal synthesis method

Hydrothermal synthesis is a heterogeneous reaction in an aqueous media occurring in a closed system above room temperature under pressure greater than 1 atm [15].

In most cases, the reaction mixture is poured into a Teflon liner and placed in a stainless-steel reactor. Such a reactor is easily assembled or dissembled, leak-proof at high temperature and pressure conditions, and inert to acids, bases, and oxidizing/reducing agents [16].

This synthesis method employs water because it is an environmentally safe and cost-effective material compared to organic solvents. Moreover, water's properties change significantly under hydrothermal conditions, favoring the crystal formation processes. For instance, the density of water under typical hydrothermal conditions decreases, which aids crystal growth since the mass transport of different solute species (ions, molecules) increases remarkably. Furthermore, the dielectric constant (the ability to store particles with a charge) of water decreases with increasing temperature and increases with increasing pressure. However, the pressure is a parameter of lower influence in controlling the dielectric constant of water, which means that electrolytes dissociated under normal conditions will tend to associate at elevated temperatures of the hydrothermal synthesis route [15-17]. Thus, water acts not only as a reaction media but, in a way, it catalyzes the reaction as well.

There are numerous scientific articles describing the hydrothermal synthesis of lanthanide orthophosphates and highlighting its advantages:

- simple lanthanide and phosphorus precursors can be used (usually salts – chlorides/nitrates and different ammonium phosphates, respectively) [8];
- particles with various morphologies (both nano and micro rods, wires, prisms, cubes, stars, spheres, etc.) are easily obtained by altering synthesis parameters [18-21];
- high monodispersity of produced particles [20, 21];
- high reproducibility [22];
- surfactant-free surface of the synthesized particles allows their further surface functionalization leading to the engineering of multimodal materials [3].

Therefore, the hydrothermal synthesis method is considered a high-ranking tool in the chemical engineering of novel luminescent, electronic, magnetic, and catalytic materials [17, 23].

1.3 Optical properties of Gd^{3+}, Ce^{3+}, Tb^{3+}, and Eu^{3+}

Gd^{3+} distinguishes itself from other trivalent lanthanide ions by having seven unpaired electrons in the f orbital (possessing electronic configuration [Xe]4f^7) and demonstrating magnetic properties. Moreover, gadolinium(III) ions have the highest energy difference (ca. 32 000 cm^{-1}) between their ground state (^{8}S) and the lowest excited state (^{6}P$_{7/2}$) if compared with the energy level structure of other trivalent lanthanide ions (see Figure 2). Consequently, sharp emission lines of Gd^{3+} ^{6}P$_J$ → ^{8}S optical transitions (where J = 3/2, 5/2, 7/2) lie in NUV region. However, they are only observed in lattices possessing a wide bandgap [24-26].

Materials containing trivalent gadolinium ions are widely used as MRI agents, host lattices for fluorescent lamp phosphors, X-ray intensifying screens, and scintillators for X-ray tomography [27-31].

Cerium(III) ion adopts the simplest electronic configuration among the optically active lanthanide ions since it possesses only one electron in the f orbital (electronic configuration [Xe]4f^1). Due to spin-orbit coupling, the [Xe]4f^1 configuration is split into two levels: ^{2}F$_{5/2}$ and ^{2}F$_{7/2}$. The energy difference between these levels is ca. 2200 cm^{-1} (see Figure 2). Since the energy difference between 5d and 4f orbitals of cerium(III) ion is relatively high, the possibility of nonradiative energy relaxation is low and, depending on the host lattice, the emission of Ce^{3+} based phosphors is typically observed in NUV or blue spectral region (5d → ^{7}F$_{5/2,7/2}$ optical transitions). However, host matrixes possessing high covalent character and strong crystal fields can shift the lowest component of Ce^{3+} 5d orbital to relatively low energies, and emission in the yellow, orange, or even red spectral region can be observed. Since Ce^{3+} [Xe]4f^1 → [Xe]5d^1 transitions are spin and parity allowed, the emission spectra of Ce^{3+} ions extend over a vast spectral range and are strongly dependent on the local surroundings of the trivalent cerium sites [32-35].

Luminescent materials containing Ce^{3+} ions are widely used in white LEDs, scintillators, lasers, and fluorescent lamps [34, 36, 37].

The terbium(III) ion possesses eight electrons in the 4f orbital, and its electronic configuration can be written as [Xe]4f^8. Due to the high number of electrons in the 4f orbital, Tb^{3+} possesses many different energy levels, $N = \dfrac{14!}{8!(14-8)!} = 3003$. Such a high number of energy levels originates from the electrostatic repulsion, spin-orbit coupling, and crystal field effects. It should be noted that Tb^{3+} emission is highly sensitive to the Tb^{3+} concentration. For instance, at low Tb^{3+} (≤0.1%) concentrations, the emission lines in the violet and blue spectral regions dominate the emission spectra. These lines originate from ^{5}D$_3$ → ^{7}F$_J$ transitions. However, it is enough to increase the Tb^{3+} concentration to 1%, and the dominant emission lines appear in the green and orange spectral regions originating from ^{5}D$_4$ → ^{7}F$_J$ transitions (see Figure 2). Such a shift is caused by the cross-relaxation process between the adjacent Tb^{3+} ions resulting in a population of ^{5}D$_4$ levels at the expense of ^{5}D$_3$ levels. The highest emission intensity is usually detected in the green spectral range due to the ^{5}D$_4$ → ^{7}F$_5$ optical transition [32, 38-40].

Terbium(III) phosphors are usually encountered in green-emitting fluorescent lamps, LEDs, and bioimaging agents [41-43].

Eu^{3+} possess six electrons in $4f$ orbital (adopts $[Xe]4f^6$ electronic configuration). This electronic configuration, parallel to Tb^{3+}, is split into many different energy levels, $N = \dfrac{14!}{6!(14-6)!} = 3003$.

When excited, europium(III) ions emit red to reddish-orange light caused by $^5D_0 \rightarrow {}^7F_{0-4}$ optical transitions (Figure 2). The IR emission from optical transitions $^5D_0 \rightarrow {}^7F_{5,6}$ is rarely observed or investigated since detectors' operating range in spectrometers is usually in the visible range. Eu^{3+} emission, similar to Tb^{3+}, is also concentration-dependent. At low Eu^{3+} ($\leq 0.1\%$) concentrations, the emission lines in the blue and green spectral regions dominate the emission spectra. These lines originate from $^5D_{2,1} \rightarrow {}^7F_J$ transitions. However, it is enough to increase the Eu^{3+} concentration to 1%, and the dominant emission lines appear in the orange and red spectral regions originating from $^5D_0 \rightarrow {}^7F_{1,2}$ transitions (see Figure 2). Again, such a shift is caused by the cross-relaxation process between the adjacent Eu^{3+} ions resulting in a population of $^5D_0$ levels at the expense of $^5D_{1,2}$ levels Eu^{3+} emission spectra contain narrow peaks since the intraconfigurational f-f transitions are parity forbidden. The electrons in the $4f$ orbital are shielded by the filled $5s$ and $5p$ orbitals (the radius of the $4f$ orbital is smaller than the radii of $5s$ and $5p$ orbitals). Therefore f-electrons are less affected by the environment of the ion. The same explanation stands for the sharp and narrow emission peaks of Gd^{3+} and Tb^{3+} [39, 40, 44, 45].

Luminophors doped with trivalent europium ions are used in red fluorescent lamps, LEDs, and as bioimaging or anti-counterfeit pigments [39, 46, 47].

Some lanthanide ions have excited states of similar energy; combining them might lead to energy transfer processes. In such a case, the emission of a particular lanthanide ion can be boosted several times. Moreover, the lanthanide ion becomes excitable in a spectral range where, if alone in the host matrix, it does not absorb. Inorganic luminescent materials doped with Ce^{3+}/Tb^{3+} or Tb^{3+}/Eu^{3+} pairs are a perfect example of such a phenomenon. In a Ce^{3+}/Tb^{3+} system, trivalent cerium ions act as sensitizers and transfer energy to the activators – trivalent terbium ions. Similarly, terbium(III) ions act as sensitizers and europium(III) ions – as activators in the Tb^{3+}/Eu^{3+} system. In such systems, one can control energy transfer efficiency by manipulating the ratio of sensitizer and activator ions. Thus the color of the phosphor's emitted light can also be tailored. Phosphors containing the Ce^{3+}/Tb^{3+} system might emit blue to green light, and the ones with the Tb^{3+}/Eu^{3+} system might emit light from green to red in [4, 5, 44]. Gd^{3+} ions are also reported as an energy transfer agent in Gd^{3+}-$Ce^{3+}/Tb^{3+}/Eu^{3+}$ systems, enhancing the emission intensity of these ions [48, 49].

Figure 2. Energy levels of Gd^{3+}, Ce^{3+}, Tb^{3+}, and Eu^{3+} ions [50, 51].

1.4 Perspectives of GdPO₄: Ln^{3+} particles in the biomedical field

As discussed in a previous chapter, the unique electronic configuration of Gd^{3+} determines its magnetic properties; therefore, various gadolinium chelates are implemented as MR contrast agents. One of such commonly applied complexes is named Magnevist® (Gd-DTPA). Gd^{3+} is highly toxic, and, unfortunately, even the chelated forms tend to release Gd^{3+} into the organism inevitably; therefore, such MR agents are considered a health hazard [52]. However, when Gd^{3+} ions are placed into an inorganic phosphate matrix, the chance of releasing these ions becomes much lower since the solubility of lanthanide phosphates is very low [53].

Moreover, due to similar lanthanide ionic radii, GdPO₄ particles are exceptionally suitable for incorporating other optically active lanthanide ions, the emission of which covers the spectral range from NUV to NIR. Registering visible or NIR emission of such particles would allow detecting various changes in different organisms at a cellular level, facilitating the diagnosis of various diseases. NUV emission of organic drug-modified lanthanide phosphate particles could be suitable for targeted drug release [54-56].

Thus, GdPO₄ particles doped with various lanthanide ions could be considered a potential multimodal biomedical material that combines MR bioimaging, conventional imaging, and drug delivery functionalities.

2. EXPERIMENTAL SECTION

2.1 Synthesis route

All samples were prepared via hydrothermal synthesis method manipulating only two parameters which are <Gd> : <P> molar ratio and the pH of the reaction mixture. Firstly, two series of undoped $GdPO_4$ samples were produced:

1. 9 samples synthesized under neutral reaction media (pH = 7) using different <Gd> : <P> molar ratios (1:7.5, 1:10, 1:12.5, 1:15, 1:17.5, 1:20, 1:25, 1:30, 1:50);
2. 9 samples synthesized under molar ratio of <Gd> : <P> = 1:10 ensuring different pH of the reaction mixture (2, 3, 4, 5, 6, 8, 9, 10, 11).

$GdPO_4$ samples doped with single Ce^{3+}, Tb^{3+} and Eu^{3+} ions or their combinations were synthesized under alkaline media of the reaction mixture (pH = 10) at a molar ratio <Gd> : <P> = 1:10. Synthesis of 3 samples of $GdPO_4$:15%Eu^{3+} phosphors differs only in the variation of chosen <Gd> : <P> molar ratio (1:10, 1:50, and 1:100).

Materials used are as follows: Gd_2O_3 (99.99%, Tailorlux), Eu_2O_3 (99.99%, Tailorlux), Tb_4O_7 (99.9%, Alfa Aesar), $Ce(NO_3)_3 \cdot 6H_2O$ (99.5%, Acros Organics), $NH_4H_2PO_4$ (≥99%, Carl Roth), tartaric acid (99.99%, Eurochemicals), nitric acid (70%, Eurochemicals), ammonium hydroxide (30%, Chempur). $Ln(NO_3)_3$ were prepared by dissolving Ln_2O_3 in diluted nitric acid.

The synthesis procedure starts with the formation of tartaric acid – Ln^{3+} complex, which was induced by mixing stoichiometric amounts of $Ln(NO_3)_3$ (0.4 M) and tartaric acid (30 mL 0.3 M) aqueous solutions. The obtained mixture was left under magnetic stirring for 30 minutes at room temperature. Afterwards, the pH of the produced solution was adjusted to 10 by adding NH_4OH solution. Subsequently, 20 mL of freshly prepared aqueous $NH_4H_2PO_4$ solution was poured at once, instantly turning the transparent reaction mixture into the turbid one. The morphology of the $GdPO_4$ nanoparticles depends on the <Gd> : <P> molar ratio; therefore, each time different concentration of $NH_4H_2PO_4$ solution was prepared since the volume of the solution was kept constant i.e., 20 mL. Furthermore, the pH of the obtained reaction mixture was again adjusted to 10 using NH_4OH solution and then diluted to 80 mL by adding DI water, followed by adjusting the pH value once again, if required. Consequently, the produced solution was left under magnetic stirring for 30 minutes at room temperature. Finally, the reaction mixture was poured into a Teflon liner and placed inside stainless steel autoclave. The hydrothermal reaction took place at 160 °C temperature furnace for 24 h, or 160 °C temperature for 12 hours, using the BERGHOF hydrothermal reactor and BTC-3000 Temperature Controller as well as Data Logger by BERGHOF (for the series of 3 samples of $GdPO_4$:15%Eu^{3+}) [3].

Synthesized particles were centrifuged four times at 10000 rpm for ten minutes. In between centrifugation cycles, particles were washed under ultrasound using DI water. The obtained powders were either dried at 70 °C for 24 hours or stored in an aqueous media.

2.2 Sample characterization

2.2.1 XRD measurements

The phase purity of prepared phosphates was examined by the X-ray diffraction (XRD) technique. XRD patterns were recorded using Rigaku MiniFlexII diffractometer operating in Bragg-

Brentano geometry in a $5° \leq 2\theta \leq 80°$ range under a Ni filtered Cu Kα radiation. The scanning step width was 0.02°, and the scanning speed was 5°/min.

2.2.2 SEM imaging

Field-emission Hitachi SU-70 Scanning Electron Microscope (SEM) images were taken to determine the morphology and size of the synthesized phosphate particles. Electron acceleration voltage – 5 kV. Particle size was measured manually (50 particles per sample) using ImageJ v1.8.0 software.

2.2.3 Excitation and emission spectra measurements

Excitation and emission spectra were recorded with Edinburgh Instruments FLS980 spectrometer (double grating Czerny-Turner excitation and emission monochromators, 450 W Xe arc lamp, single-photon counting photomultiplier Hamamatsu R928P). A detailed description of spectra recording parameters for each sample (λ_{ex}, λ_{em}, excitation, and emission slits) is presented in Table S1 (Appendix 1). Each spectrum was recorded with 0.5 nm step width and 0.2 s dwell (integration) time. Emission spectra were corrected for instrument response using the correction file provided by Edinburgh Instruments. Excitation spectra were corrected by a reference detector.

2.2.4 PL decay measurements

PL decay curves were recorded with Edinburgh Instruments FLS980 spectrometer using a μ-flash lamp (μF2) as an excitation source, pulse repetition rate was 25 Hz. For recording Ce^{3+} PL decay curves, a hydrogen-filled nano-flash lamp (nF920) was used as an excitation source; the pulse repetition rate was 40 kHz. λ_{ex} and λ_{em} values for each sample are summarized in Table S2 (see Appendix 1).

2.2.5 Thermal quenching measurements

Temperature-dependent excitation and emission spectra, PL decay curves were also recorded with Edinburgh Instruments FLS980 spectrometer employing cryostat "MicrostatN" from the Oxford Instruments (cooling agent – liquid nitrogen) for the temperature control. All measurements were conducted at 77 K and in the range from 100 to 500 K in 50 K intervals (stabilization time was 120 s, and temperature tolerance was set to ±5 K).

$TQ_{1/2}$ (the temperature at which a luminescent material loses half of its emission efficiency) and E_a (activation energy – the amount of energy that must be given to induce thermal quenching) values for the synthesized samples were calculated using the following equations:

$$I(T) = \frac{I_0}{1 + Be^{-\frac{E_a}{k_b T}}} \qquad \text{(Eq. 1)}$$

$$TQ_{1/2} = -\frac{E_a}{k_b \ln\frac{1}{B}} \qquad \text{(Eq. 2)}$$

where $I(T)$ – normalized integrated emission value at a certain temperature (T); I_0 – the highest normalized integrated emission value (in this case equal to 1); B – quenching frequency factor; k_b – Boltzmann constant equal to $8.6173 \cdot 10^{-5}$ eV/K [57].

2.2.6   BET measurements

The surface area of produced $GdPO_4$:15%Eu^{3+} samples was examined by conducting a nitrogen gas adsorption via Brunauer – Emmet – Teller (BET) method using a surface area and porosity analyzer TriStar II 3020.

2.2.7   Biotoxicity tests of $GdPO_4$:15%Eu^{3+} NPs

Daphnia Magna neonates, taken from laboratory culture, were used for inhibition assays performed according to ISO 6341:2012 standard and OECD recommendations for acute toxicity tests of Daphnia species. Six test concentrations of different type of $GdPO_4$:15%Eu^{3+} NPs (3.125, 6.25, 12.5, 25, 50, and 100 µg/mL) plus a control (0 µg/mL) were used. In all experiments, deep-well water was used as dilution water (pH = 8.2).

For each NPs concentration, ten neonates (< 24 h old) from a designated brood were placed in 50 mL glass beakers for 24 h containing 20 mL of test solution. Before analysis, *Daphnia Magna* were cultivated in Elendt M4 medium at 21 ±0.5 °C [58]. The daphnids were maintained at a constant temperature at 16:8 hours light:dark cycle in the climate cabinet (PGC-660, Bronson, Zaltbommel, The Netherlands). The test solution was not renewed, and *Daphnia Magna* were not fed during the testing period. After the exposure of 24 hours, the mortality for the individuals in each glass beaker was assessed (those animals whose heartbeats have stopped are considered dead). All experiments were conducted in triplicate.

In order to count the heart rates, a live *Daphnia Magna* was placed on an objective slide with a drop of solution with the respective NPs concentration. The heart rate of a single *Daphnia Magna* was measured in 10 s periods for 15 minutes using an optical microscope (Optika B-600TiFL (Italy) equipped with a digital camera (Leica, Germany)) at x4 magnification. Heart rate was finally counted manually in the low-speed play condition.

The LC_{50} values (i.e., the lethal concentration which kills 50% of a *Daphnia Magna* population tested) were calculated by the trimmed Spearman-Karber method using mortality rates (%) [59]. The toxicity data analysis was performed using STATISTICA software (10.0 Software, Inc. PA, USA).

3. RESULTS AND DISCUSSION

3.1 Structural properties of GdPO$_4$ samples

3.1.1 XRD measurements

XRD patterns of the produced undoped GdPO$_4$ samples match well with the reference pattern under any chosen <Gd> : <P> molar ratio or pH of the reaction mixture (Figure 3). This indicates that phase pure trigonal particles (space group P3$_1$21) were obtained. A broad diffraction band in the range of $5° \leq 2\theta \leq 40°$ is observed due to the amorphous glass sample holder used during measurements.
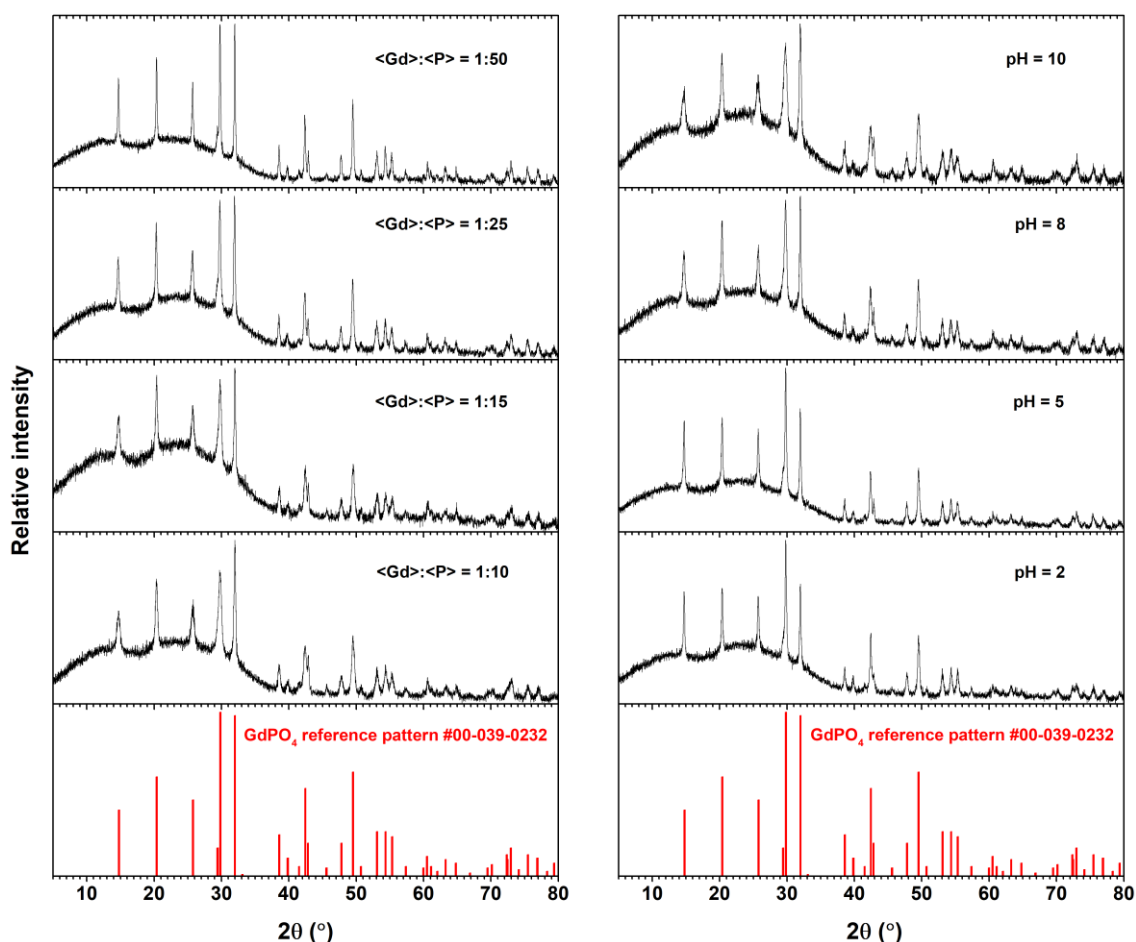
Figure 3. XRD patterns of the synthesized GdPO$_4$ particles under different synthesis conditions: neutral reaction media (pH = 7) with different <Gd> : <P> molar ratio (left) and molar ratio <Gd> : <P> = 1:10 with different pH of the reaction mixture (right).

3.1.2 SEM images

Figure 4 presents SEM images of GdPO$_4$ particles synthesized under neutral reaction media (pH = 7) changing only the <Gd> : <P> molar ratio. These images show that wider nanorods are obtained with an increasing <Gd> : <P> molar ratio. SEM images depicted in Figure 5 reveal that the length of GdPO$_4$ rods tend to decrease from sub-micro to nano dimensions with pH value increasing

from acidic to alkaline. Thus, the pH of the reaction media has a substantially greater effect on the size of the synthesized phosphates compared to the effect of the <Gd> : <P> molar ratio.
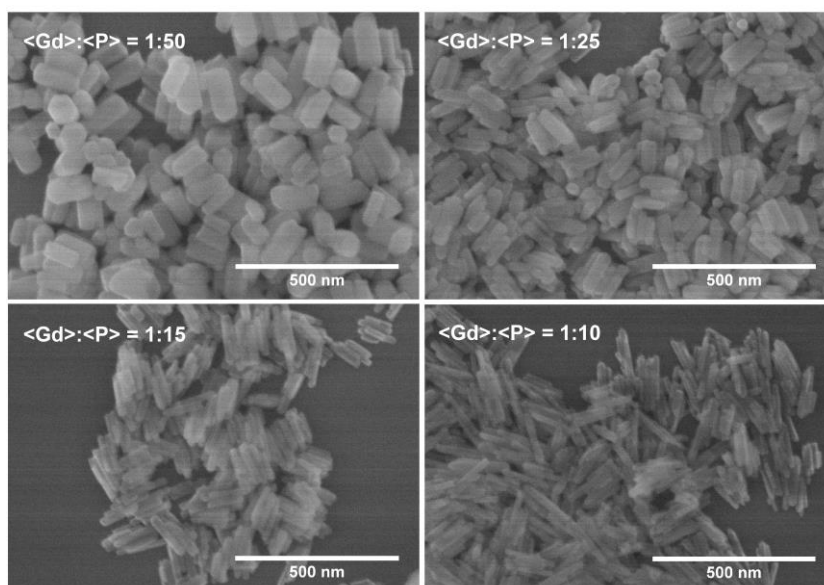
Figure 4. SEM images of GdPO$_4$ nanoparticles prepared under different molar <Gd>:<P> ratio at a neutral reaction mixture (pH = 7).
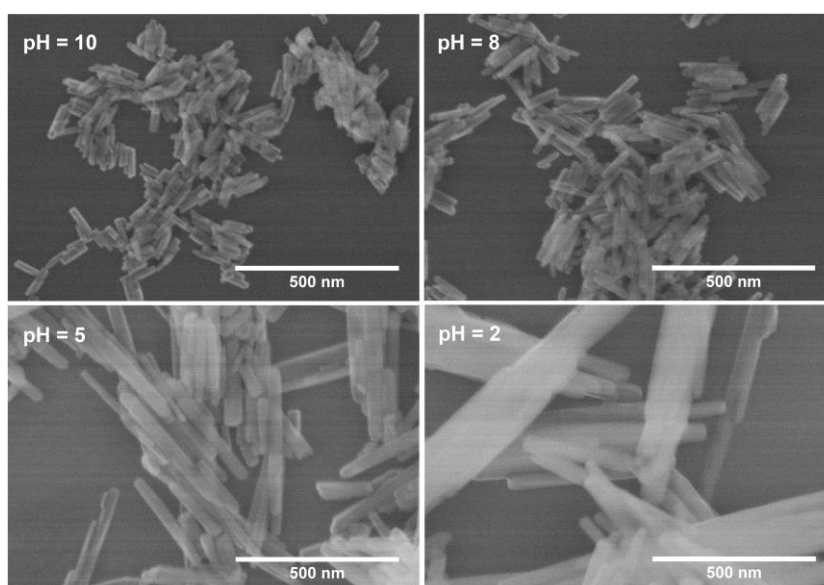
Figure 5. SEM images of GdPO$_4$ nanoparticles prepared under different pH of the reaction mixture at a fixed <Gd> : <P> molar ratio (1:10).

SEM images of the synthesized GdPO$_4$ samples were also used to calculate average size of the produced particles (see Tables S3 and S4 in Appendix 2). The obtained results are depicted graphically as a function of <Gd> : <P> molar ratio (Figure 6a), and as a function of the pH of the reaction mixture (Figure 6b). With increasing <Gd> : <P> molar ratio, the average particle length and its dispersion tend to decrease. However, from molar ratio <Gd> : <P> = 1:20, the reverse effect was observed. On the contrary, the average particle width and dispersion tend to increase with increasing

<Gd> : <P> molar ratio. As for increasing the pH value of the reaction media, both the length and width of the phosphate particles and their dispersions tend to decrease.

The smallest and the most monodisperse GdPO$_4$ nanorods were obtained under molar ratio <Gd> : <P> = 1:10 at a pH = 10. Their average length is equal to ca. 81 nm, and their average width is ca. 17 nm. Therefore, these conditions were chosen to synthesize GdPO$_4$ nanoparticles doped with single Ce^{3+}, Tb^{3+} and Eu^{3+} and their different combinations.
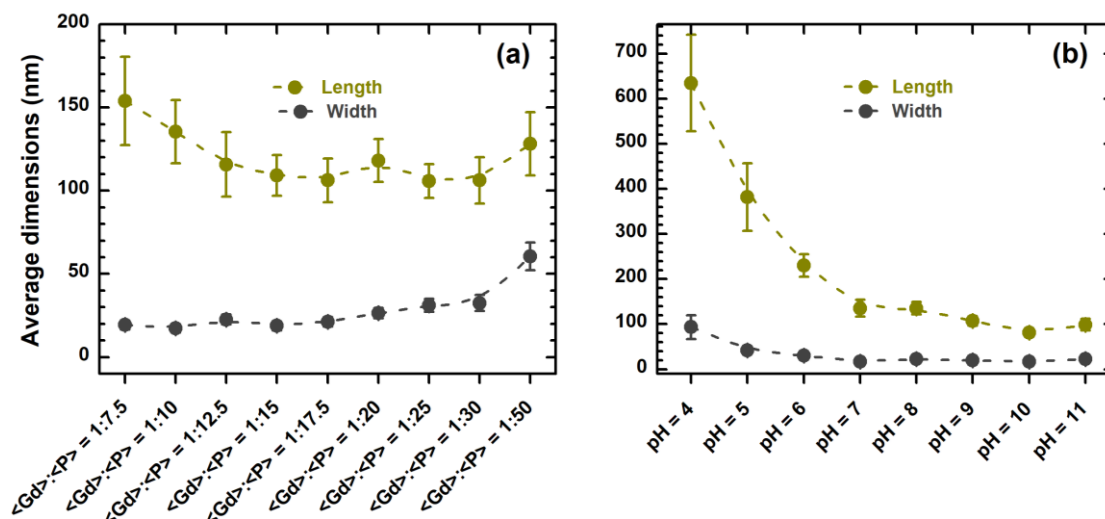
Figure 6. Average dimensions of GdPO$_4$ particles as a function of <Gd> : <P> molar ratio (a) and as a function of the pH of the reaction mixture (b).

3.2 Structural and morphological properties of GdPO$_4$ particles doped with single lanthanide ions

3.2.1 XRD measurements and SEM images of GdPO$_4$:Ce^{3+} samples

Since the XRD patterns of all five GdPO$_4$:Ce^{3+} samples (where the concentration of Ce^{3+} is equal to 5%, 10%, 20%, 25%, and 50%) match the reference pattern well, the produced particles possess trigonal crystal structure without any impurity phases (see Figure 7). In this case, VIII coordinated Gd^{3+} with an ionic radius of 1.053 Å are replaced by VIII coordinated Ce^{3+} with an ionic radius of 1.143 Å (larger by 8.55%) [13]. The relatively small mismatch between ionic radii obeys Vegard's law, which states that solid solution formation is possible only if the ionic radii of ions replacing one another in the crystal lattice differ by less than 15% [60]. Furthermore, as the concentration of Ce^{3+} ions increase the broader the peaks of XRD patterns were recorded, indicating that smaller particles tend to form. Such peak broadening is present because periodic atomic arrangements that generate the sharp diffraction peak profile are limited when the measured particles are of nanoscale dimensions [61].
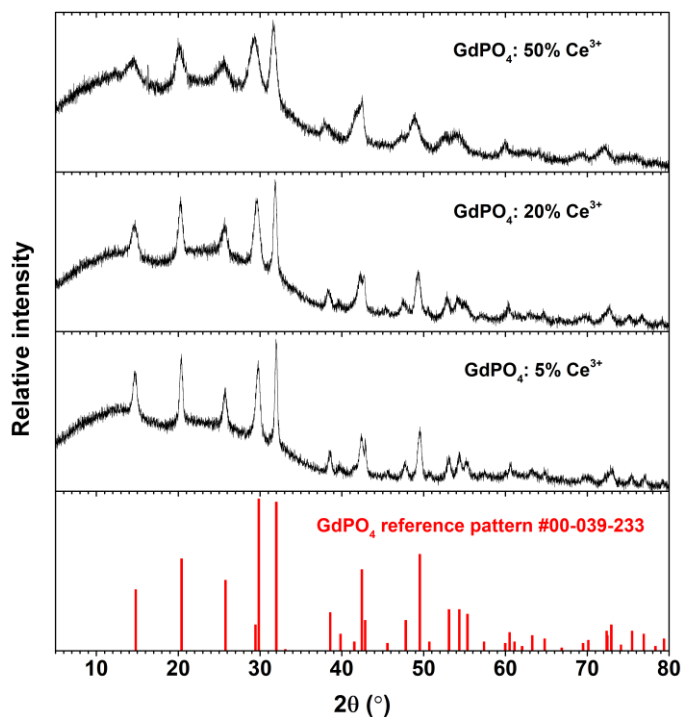
Figure 7. XRD patterns of $GdPO_4:Ce^{3+}$ samples as a function of Ce^{3+} concentration.

Figure 8 shows SEM images of $GdPO_4:5\%Ce^{3+}$ (a) and $GdPO_4:50\%Ce^{3+}$ nanorods (b). It is evident that smaller nanoparticles tend to form as the amount of Ce^{3+} ions in the phosphate matrix increases. The calculated average particle size values are presented in Table S5 (Appendix 2). The average length of $GdPO_4:Ce^{3+}$ nanorods decreases from ca. 59 nm to ca. 29 nm as the concentration of Ce^{3+} increases from 5% to 50%. The average width of these particles decreases from ca. 29 nm to ca. 9 nm, respectively. Thus, smaller $GdPO_4$ NPs form if Ce^{3+} is introduced into the crystal lattice.
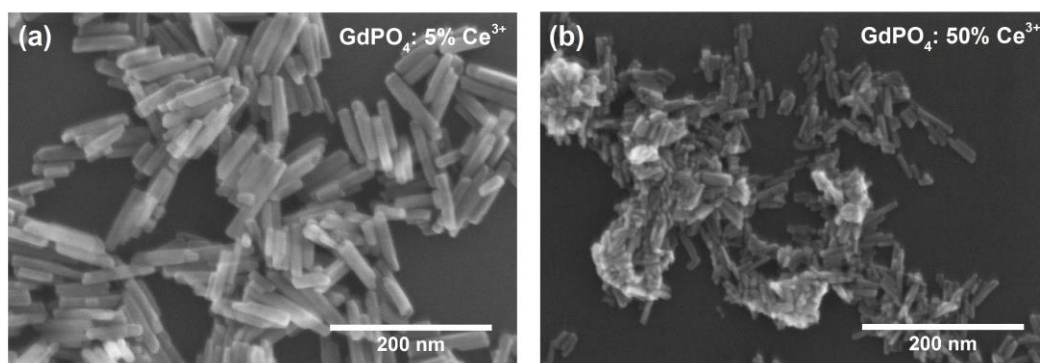
Figure 8. SEM images of $GdPO_4:Ce^{3+}$ samples doped with 5% Ce^{3+} (a) and 50% Ce^{3+} (b).

3.2.2 XRD measurements and SEM images of $GdPO_4:Tb^{3+}$ samples

XRD patterns of all five $GdPO_4: Tb^{3+}$ samples (where the concentration of Tb^{3+} ions is equal to 1%, 5%, 10%, 20%, and 50%) match well with the trigonal reference pattern and no phase impurities are present (see Figure 9). Here, Gd^{3+} (CN = 8, R = 1.053 Å) are replaced by Tb^{3+} (CN = 8, R = 1.040 Å) which is 1.25% smaller [13], and the ionic radii mismatch obeys Vegard's law [60].
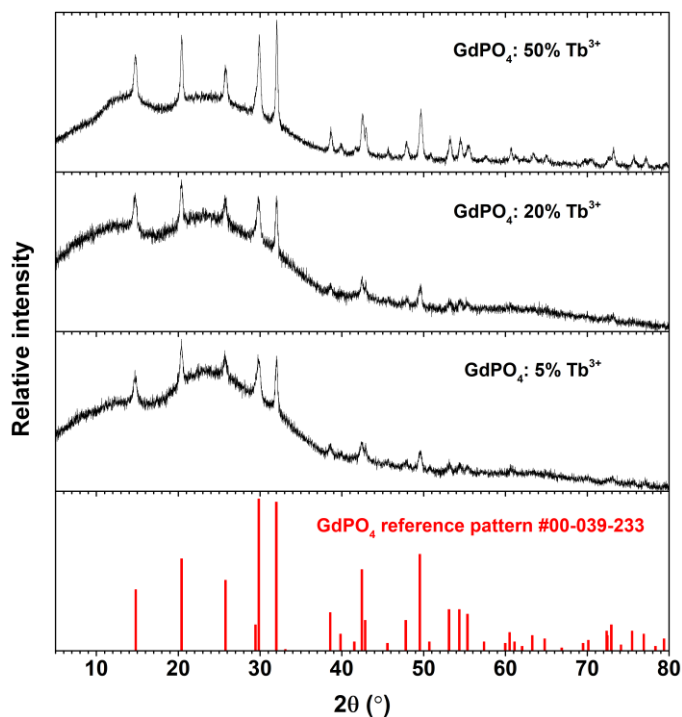
Figure 9. XRD patterns of GdPO$_4$:Tb^{3+} samples as a function of Tb^{3+} concentration.

SEM images of GdPO$_4$ nanorods doped with 1%Tb^{3+} and 50%Tb^{3+} are given in Figures 10a and 10b, respectively. The calculated average particle size values are tabulated in Table S6 (see Appendix 2). The average GdPO$_4$:Tb^{3+} nanorods length increases from ca. 75 nm to ca. 89 nm as the concentration of Tb^{3+} increases from 1% to 50%, respectively, whereas the average width of these NPs only slightly increases from ca. 19 nm to ca. 20 nm following the same trend. However, these changes in Tb^{3+} doped samples dimensions fall within the limits of standard deviations. Therefore, it could be stated that the introduction of Tb^{3+} into the GdPO$_4$ crystal lattice does not cause significant changes in the size of obtained nanorods in comparison with undoped GdPO$_4$, where the average length is ca. 81 nm and the average width ca. 17 nm.
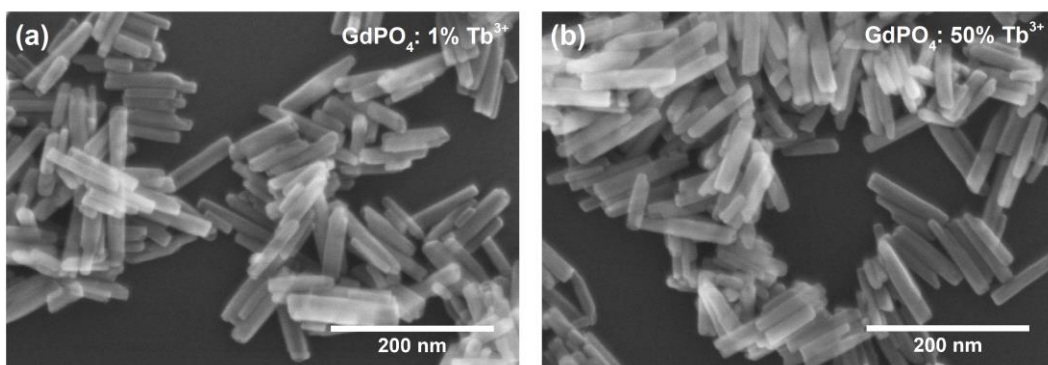
Figure 10. SEM images of GdPO$_4$:Tb^{3+} samples doped with 1% Tb^{3+} (a) and 50% Tb^{3+} (b).

3.2.3 XRD measurements and SEM images of GdPO$_4$:Eu^{3+} samples

Figure 11 depicts XRD patterns of three out eight synthesized GdPO$_4$: Eu^{3+} samples (the Eu^{3+} concentration in 8 samples was 0.5%, 1%, 2.5%, 5%, 7.5%, 10%, 20%, and 50%). The given XRD

patterns match the reference pattern well and indicate that produced materials contain trigonal crystal structure with no impurity phases present. Again, the VIII coordinated Gd^{3+} ions (R = 1.053 Å) are replaced by VIII coordinated Eu^{3+} (R = 1.066 Å), which is only 1.23% larger [13] and within the limits of the solid solution formation range determined by already mentioned Vegard's law [60].
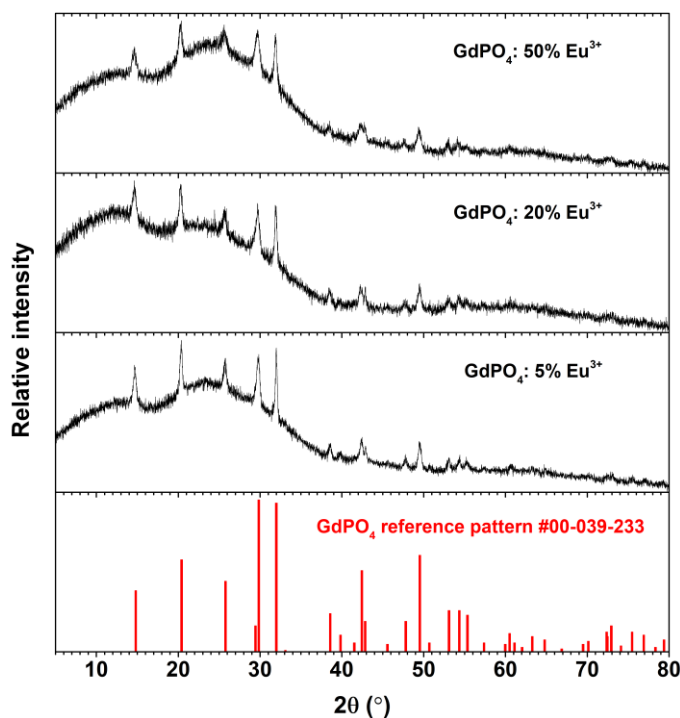
Figure 11. XRD patterns of $GdPO_4$:Eu^{3+} samples as a function of Eu^{3+} concentration.

SEM images of $GdPO_4$:1%Eu^{3+} and $GdPO_4$:50%Eu^{3+} nanorods are demonstrated in Figures 12a and 12b, respectively. The calculated average particle size values are given in Table S7 (see Appendix 2). The average length of $GdPO_4$: Eu^{3+} nanorods decreases from ca. 88 nm to ca. 74 nm when the concentration of Eu^{3+} increases from 1% to 50%, respectively. The average width of these particles also decreases from ca. 21 nm to ca. 18 nm following the same trend. Nevertheless, these particle length and thickness changes occur within the limits of standard deviation. Therefore, analogously to Tb^{3+} doped samples, incorporation of Eu^{3+} into $GdPO_4$ NPs does not cause significant changes in the size of obtained nanorods.
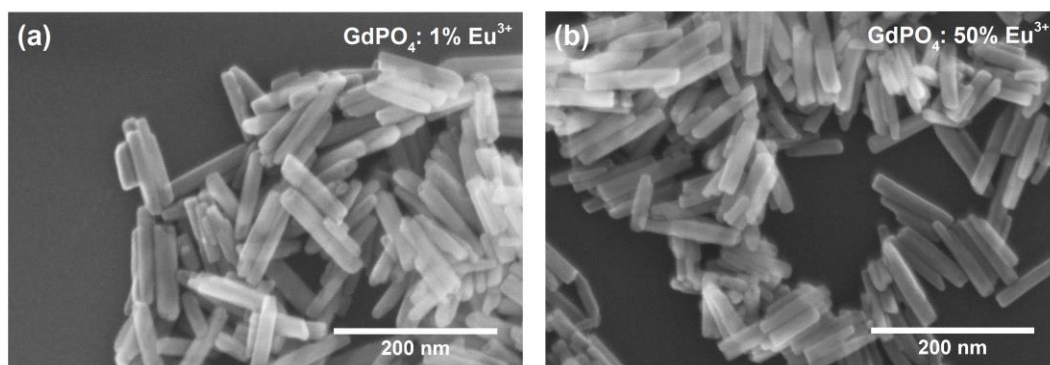
Figure 12. SEM images of $GdPO_4$:Eu^{3+} samples doped with 1% Eu^{3+} (a) and 50% Eu^{3+} (b).

3.3 Optical properties of GdPO₄ particles doped with single lanthanide ions

3.3.1 Excitation and emission spectra of GdPO₄:Ce³⁺ samples

GdPO$_4$:Ce^{3+} excitation spectra (λ_{em} = 360 nm) are given in Figure 13a. The spectra contain one broad band with a maximum at ca. 275 nm. Since the spectra are not symmetric, it can be concluded that they arise from interconfigurational $^7F_{5/2} \rightarrow 5d_{1,2,3}$ optical transitions that are heavily overlapped (here $5d_{1,2,3}$ represent the different energy 5d orbitals split in the crystal field). It was observed that the excitation band intensity steadily decreases with increasing Ce^{3+} amount in the GdPO$_4$ matrix from 5% to 50%.

Figure 13b shows the broadband emission spectra (λ_{ex} = 275 nm) of Ce^{3+} doped phosphates. The emission peaks at ca. 344 nm. The emission spectra are not symmetrical and could be deconvoluted to two Gaussian curves, which represent the emission from the lowest energy component of 5d orbital ($5d_1$) to the spin-orbit split ground state of Ce^{3+}, i.e., $5d_1 \rightarrow {}^7F_{5/2}$ and $5d_1 \rightarrow {}^7F_{7/2}$ optical transitions. Similarly to the intensity of excitation spectra, the intensity of emission spectra also tends to decrease with increasing Ce^{3+} amount in the phosphor (see Figure 13c). In fact, the emission intensity drops by 63% as the concentration of Ce^{3+} increases from 5% to 50%.

In regard with Ce$^{3+} \rightarrow$ Tb^{3+} and Ce$^{3+} \rightarrow$ Eu^{3+} energy transfer investigation, the amount of Ce^{3+} in further samples (GdPO$_4$:Ce^{3+},Tb^{3+}; GdPO$_4$:Ce^{3+},Eu^{3+} and GdPO$_4$:Ce^{3+},Tb^{3+},Eu^{3+}) was chosen to be 20%. GdPO$_4$:20%Ce^{3+} sample demonstrated mediocre emission intensity if compared to 5% and 10% Ce^{3+} doped samples. However, relatively high Ce^{3+} (which will act as a sensitizer) concentration is required for efficient transfer energy to Tb^{3+}. On the other hand, the selected Ce^{3+} concentration (20%) is still low enough to avoid or at least reduce the emission quenching caused by MMCT (Ce^{3+} + Eu$^{3+} \leftrightarrow$ Ce^{4+} + Eu^{2+}).

Figure 13. Excitation (a) and emission (b) spectra of GdPO$_4$:Ce^{3+} samples; normalized integrated emission intensity as a function of Ce^{3+} concentration (c).

3.3.2 PL decay of GdPO₄:Ce³⁺ samples

Figure 14 demonstrates the PL decay curves (λ_{ex} = 275 nm, λ_{em} = 350 nm) of GdPO$_4$:Ce^{3+} phosphors and their average $\tau_{1/e}$ values (inset) as a function of Ce^{3+} concentration. Regardless of the Ce^{3+} concentration in the material, the Ce^{3+} PL decay was best fit with tri-exponential function (Eq. 3):

$$I(t) = A + B_1 e^{\frac{t}{\tau_1}} + B_2 e^{\frac{t}{\tau_2}} + B_3 e^{\frac{t}{\tau_3}} \qquad \text{(Eq. 3)}$$

where $I(t)$ – PL intensity at a given time t; A, $B_{1,2,3}$ – constants; $\tau_{1,2,3}$ – PL lifetime values [40].

The obtained $\tau_{1,2,3}$ values with standard deviations and relative shares (%) together with calculated average PL lifetime values of GdPO$_4$:Ce^{3+} samples are presented in Table S12 (Appendix 3). 10% Ce^{3+} doped sample possessed the highest average $\tau_{1/e}$ value (ca. 126 ns). From that point, the average $\tau_{1/e}$ values tend to drop as the concentration of Ce^{3+} in the phosphates increases. The decrease of average PL lifetime values is associated with the concentration quenching and the lowest average PL lifetime value (ca. 11 ns) was obtained for the sample doped with 50% Ce^{3+}.
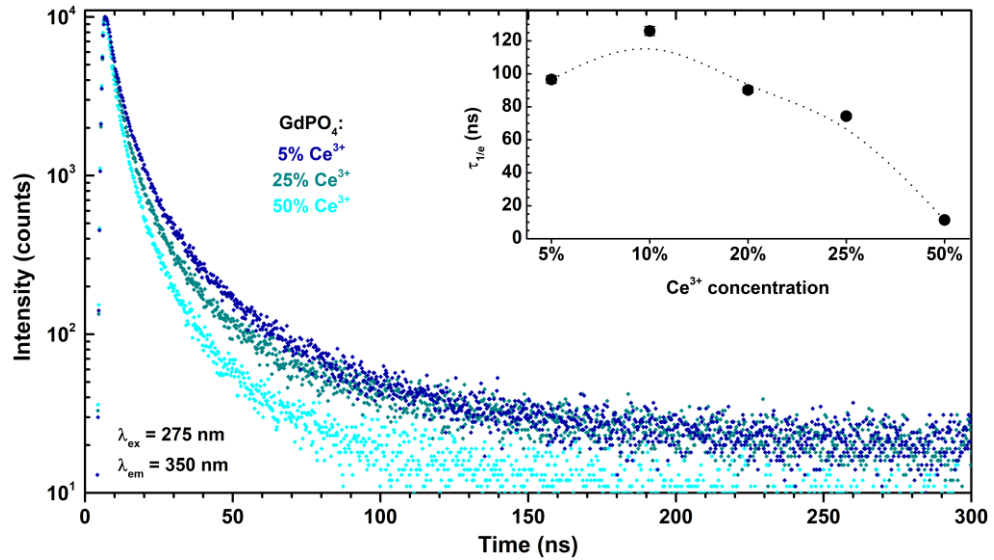
Figure 14. PL decay curves of GdPO$_4$:Ce^{3+} particles and average $\tau_{1/e}$ values (inset) as a function of Ce^{3+} concentration.

3.3.3 Thermal impact on optical characteristics of GdPO$_4$:20%Ce^{3+} samples

Both excitation and emission spectra intensity of GdPO$_4$:20%Ce^{3+} phosphor tends to significantly decrease as the temperature increases from 77 to 500 K (see Figures 15a and 15b). The normalized integrated emission intensity as a function of temperature (Figure 15c) was used to calculate TQ$_{1/2}$ and E$_a$ values, which were equal to 326 ±11 K and 0.118 ±0.017 eV, respectively.

Furthermore, tri-exponential PL decay curves fade away faster as the temperature increases. The average PL lifetime values drop from ca. 8.11 ns to ca. 1.17 ns (data presented in Table S13, Appendix 3) as the temperature rises from 100 to 500 K, respectively (see Figures 14c and 14d).

All in all, the temperature-dependent spectroscopic properties of 20% Ce^{3+} doped sample revealed that these nanorods significantly suffer from the thermal quenching which is likely caused by high Ce^{3+} concentration and high particle surface area.

Figure 15. Temperature-dependent excitation (a) and emission (b) spectra with normalized integrated emission intensity as a function of temperature (inset); temperature dependent PL decay curves (c) and calculated average $\tau_{1/e}$ values as a function of temperature (d) of GdPO$_4$:20%Ce^{3+} phosphor.

3.3.4   Excitation and emission spectra of GdPO$_4$:Tb^{3+} samples

Differently to Ce^{3+} doped phosphates, GdPO$_4$:Tb^{3+} samples demonstrate intraconfigurational f-f optical transitions (Figure 16 a,b). Both excitation (λ_{em} = 542 nm) and emission (λ_{ex} = 340 nm) spectra consist of typical Tb^{3+} optical transitions (Figure 2). However, excitation spectra contain optical transitions not only the ones from Tb^{3+} but also from Gd^{3+}. This indicates that Gd$^{3+} \rightarrow$ Tb^{3+} energy transfer occurs.

GdPO$_4$:Tb^{3+} emission spectra peak at 542 nm ($^5D_4 \rightarrow {}^7F_5$ transition) and the overall emission intensity increases as the Tb^{3+} concentration in the material goes up to 20%. However, the emission intensity drops by 18% if the Tb^{3+} concentration is increased to 50% (see Figure 16c). The decrease in emission intensity is caused by concentration quenching as a result of increased probability of cross-relaxation processes between adjacent Tb^{3+} ions (for instance, $^5D_3 + {}^7F_6 \rightarrow {}^5D_4 + {}^7F_0$) [40].

In regard with Tb$^{3+} \rightarrow$ Eu^{3+} energy transfer investigation, the amount of Tb^{3+} in further samples (GdPO$_4$:Tb^{3+},Eu^{3+} and GdPO$_4$:Ce^{3+},Tb^{3+},Eu^{3+}) was set to 20%. This sample demonstrated the highest overall emission intensity; therefore, it is expected that it will efficiently transfer energy to Eu^{3+}.
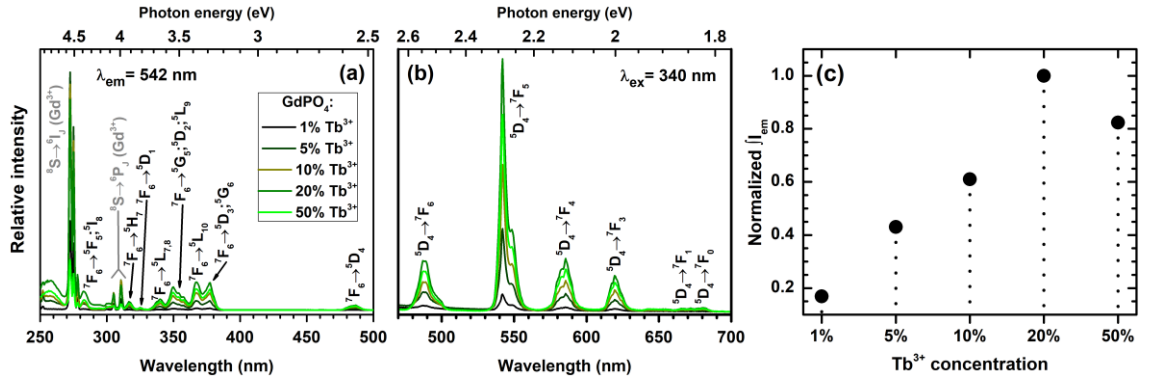
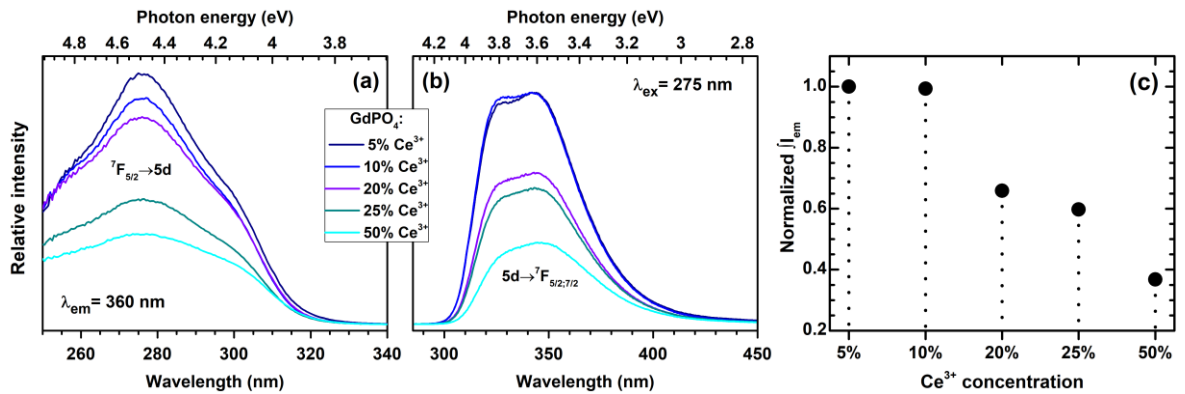**Figure 16.** Excitation (a) and emission (b) spectra of GdPO$_4$:Tb^{3+} samples; normalized integrated emission intensity as a function of Tb^{3+} concentration (c).

3.3.5 PL decay of GdPO$_4$:Tb^{3+} samples

The PL decay curves (λ_{ex} = 340 nm, λ_{em} = 542 nm) of GdPO$_4$:Tb^{3+} samples and their average PL lifetime values as a function of Tb^{3+} concentration are depicted in Figure 17. The PL decay curves which were best fit with two-exponential function (Eq.4) become steeper with increasing Tb^{3+} concentration indicating decreasing PL lifetime values. Tb^{3+} PL decay curves were best fit with triexponential function. The obtained $\tau_{1,2,3}$ values with standard deviation values and relative shares (%) and calculated average $\tau_{1/e}$ values of GdPO$_4$:Tb^{3+} samples are presented in Table S14 (see Appendix 3). The average PL lifetime values of Tb^{3+} emission at 542 nm decrease from ca. 4.24 ms to ca. 0.98 ms as the amount of Tb^{3+} ions in the phosphor increase from 1% to 50%.

$$I(t) = A + B_1 e^{\frac{t}{\tau_1}} + B_2 e^{\frac{t}{\tau_2}} \qquad \text{(Eq. 4)}$$

*I(t)* – PL intensity at a given time *t*; *A, B$_{1,2}$* – constants; *τ$_{1,2}$* – PL lifetime values [40].
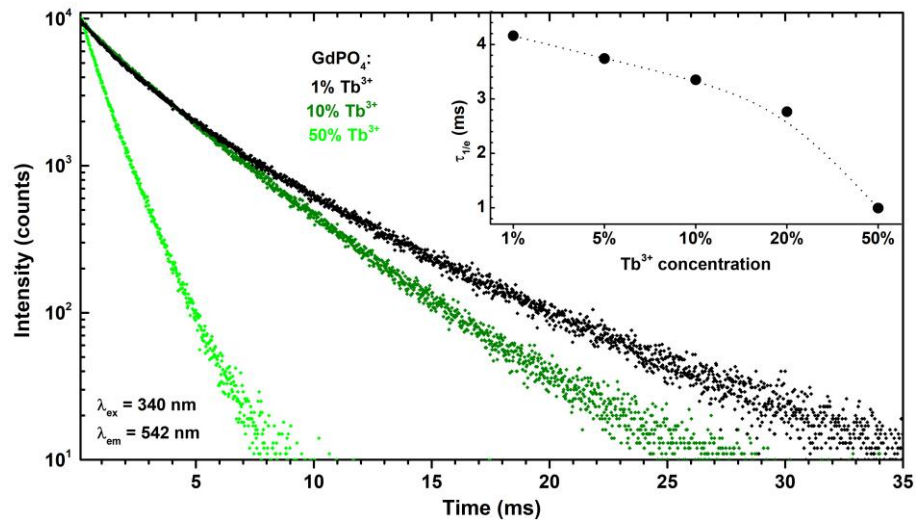
Figure 17. PL decay curves of GdPO$_4$:Tb^{3+} particles and average PL $\tau_{1/e}$ values as a function of Tb^{3+} concentration (inset).

3.3.6 Thermal impact on optical characteristics of GdPO$_4$:20%Tb^{3+} samples

Figures 18a and 18b show the decrease of GdPO$_4$:20%Tb^{3+} of excitation and emission intensity as the temperature increases from 77 to 500 K. At 500 K most of the Tb^{3+} excitation lines become barely detectable. However, the excitation lines originating from Gd^{3+} transitions are clearly visible, indicating that Gd^{3+} → Tb^{3+} energy transfer still occurs regardless of the high temperature. The emission intensity of the strongest emission line ($^5D_4$ → $^7F_5$) decreases more than twice if the temperature is increased from 77 to 500 K. However, the intensity of some emission transitions (e.g., $^5D_4$ → $^7F_1$, $^5D_4$ → $^7F_0$) decreases even faster becoming barely noticeable at 500 K. The inset of Figure 18b shows normalized integrated emission intensity as a function of temperature together with calculated TQ$_{1/2}$ and E$_a$ values of 457 ±13 K and 0.064 ±0.005 eV, respectively.

It is interesting to note that two-exponential PL decay curve at 500 K fades away slower if compared to the one measured at 77 K (see Figure18c). Such phenomenon is rather unusual in luminescent materials since increasing the temperature in most cases induces nonradiative processes leading to a decrease of the excited state lifetime. The calculated temperature-dependent average PL lifetime values are depicted in Figure 18d and summarized in Table S15 (see Appendix 3). It is evident that up to 350 K the average PL lifetime values are virtually the same. However, they increase substantially once the temperature reaches 400 K, i.e., from ca. 2.84 ms at 350 K to ca. 5.00 ms at 400 K. The synthesized particles GdPO$_4$:20%Tb^{3+} nanoparticles possess large surface area that inevitably contains many defects, which, in turn, can act as electron traps. At a specific temperature the trapped electrons can be released giving the rise in emission intensity and, thus, increasing the PL lifetime values. To test this hyphotesis one should measure the temperature-dependent afterglow properties. Unfortunately, such measurement setup is not available at Vilnius University. Besides, such measurements are outside the scope of this thesis.
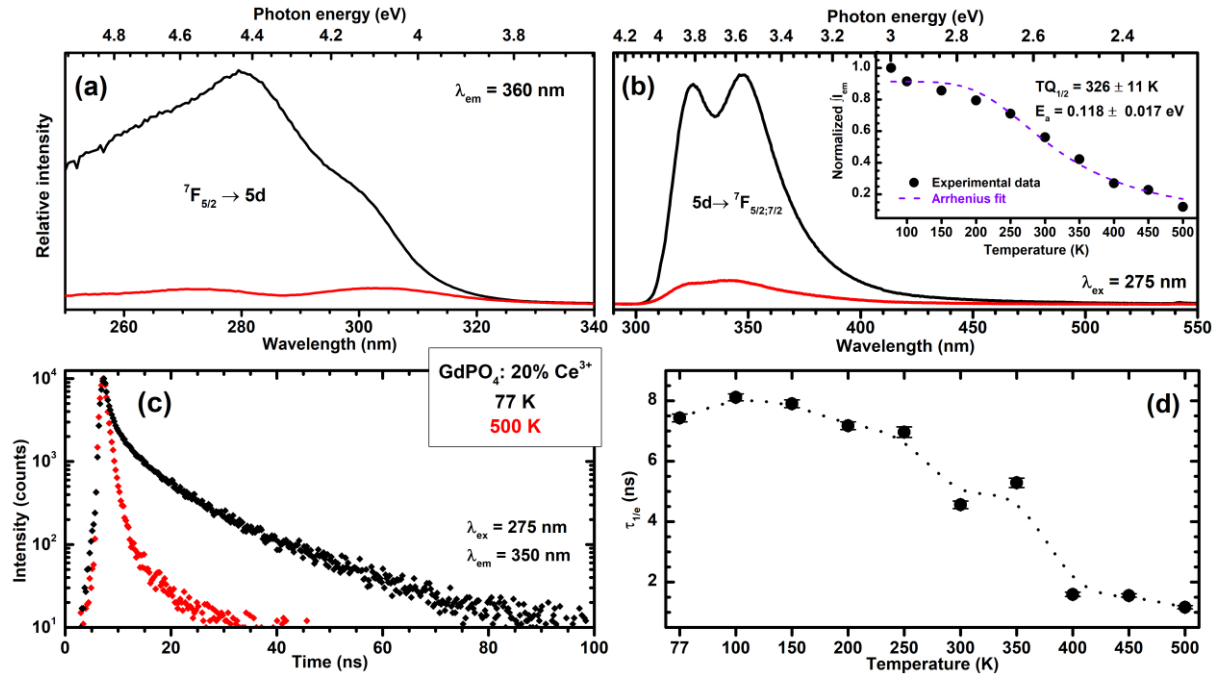

Figure 18. Temperature-dependent excitation (a) and emission (b) spectra with normalized integrated emission intensinty as a function of temperature (inset); temperature-dependent PL decay curves (c) and average $\tau_{1/e}$ values as a function of temperature (d) of GdPO$_4$:20%Tb^{3+} phosphor.

3.3.7 Excitation and emission spectra of GdPO$_4$:Eu^{3+} samples

Both excitation (λ_{em} = 587.5 nm) and emission (λ_{ex} = 393 nm) spectra of GdPO$_4$:Eu^{3+} phosphors consist of typical intraconfigurational Eu^{3+} *f-f* optical transitions and ligand to metal charge transfer (CT) band (O^{2-} → Eu^{3+}) (see Figure 19 a,b) [62]. As encountered when analyzing excitation spectra of Tb^{3+} ions doped phosphates, optical transitions of Gd^{3+} ions are also observed in the excitation spectra of GdPO$_4$:Eu^{3+} samples when monitoring Eu^{3+} emission. Therefore, it can be concluded that Gd^{3+} → Eu^{3+} energy transfer occurs in these phosphors. This can be confirmed, at least in part, by analyzing the intensity of Gd^{3+} lines in excitation spectrum (Figure 18a). The intensity of Gd^{3+} excitation lines (ca. 272 nm) is the highest when Eu^{3+} concentration is the lowest, i.e., 1%. Moreover, the intensity of Gd^{3+} excitation lines gradually decrease with increasing Eu^{3+} concentration. At the same time the concentration of Gd^{3+} decreases; thus, there are less Gd^{3+} that could transfer the energy to Eu^{3+} resulting in decrease of Gd^{3+} excitation line intensity.

The most intensive excitation line in GdPO$_4$:Eu^{3+} excitation spectra is at 393 nm ($^7F_0 \rightarrow {}^5L_6$ optical transition) and the most intensive line in emission spectra is at 694.5 nm ($^5D_0 \rightarrow {}^7F_4$ optical transition). With the increasing amount of Eu^{3+} in the material, the overall emission intensity increases and reaches the highest value for the GdPO$_4$:50%Eu^{3+} phosphor, i.e., the emission intensity increases by 87% if compared to GdPO$_4$:1%Eu^{3+} sample (see Figure 19c).
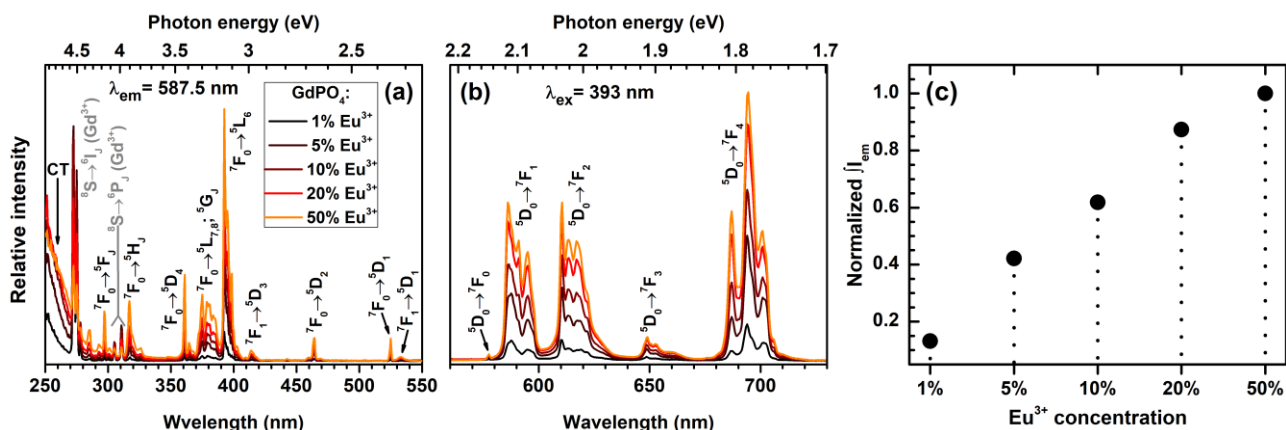
Figure 19. Excitation (a) and emission (b) spectra of GdPO$_4$:Eu^{3+} samples; normalized integrated emission intensity as a function of Eu^{3+} concentration (c).

3.3.8 PL decay of GdPO$_4$:Eu^{3+} samples

Figure 20 demonstrates PL decay curves (λ_{ex} = 393 nm, λ_{em} = 587.5 nm) of GdPO$_4$: Eu^{3+} samples and their average $\tau_{1/e}$ values as a function of Eu^{3+} concentration. GdPO$_4$: Eu^{3+} NPs showed two-exponential PL decay at any Eu^{3+} concentration (Eq. 4).

The exact calculated $\tau_{1,2,3}$ values, their standard deviation values, and relative shares (%) as well as the average PL lifetime values of GdPO$_4$:Eu^{3+} samples are given in Table S17 (see Appendix 3). Due to concentration quenching processes PL lifetime of Eu^{3+} emission at 587.5 nm decreases from ca. 3.02 ms to ca. 0.60 ms as the concentration of Eu^{3+} ions in the NPs increase from 0.5% to 50% (inset of Figure 20).
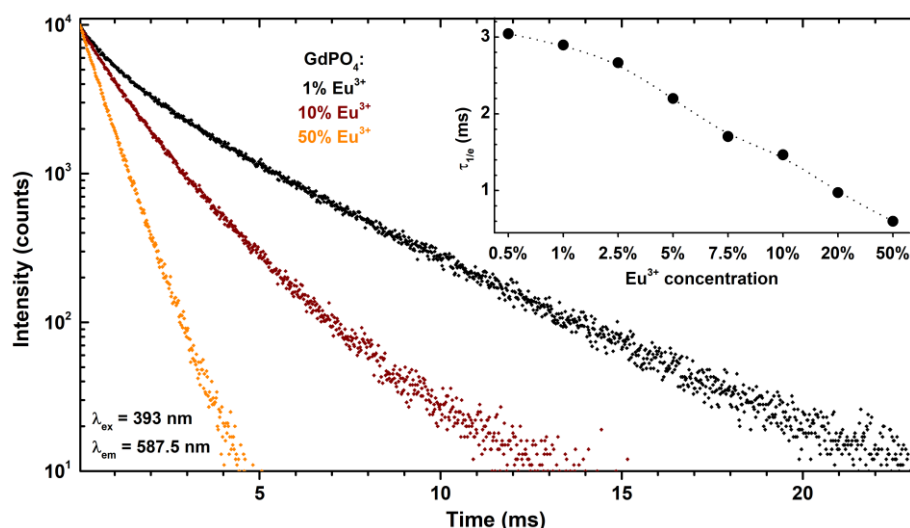
Figure 20. PL decay curves of GdPO$_4$:Eu^{3+} particles and calculated $\tau_{1/e}$ values as a function of Eu^{3+} concentration (inset).

3.3.9 Thermal impact on optical characteristics of GdPO$_4$:50%Eu^{3+} samples

Figures 21a and 21b show that the intensity of both excitation and emission spectra of GdPO$_4$:50%Eu^{3+} sample drops dramatically when the temperature increases from 77 to 500 K. The normalized integrated emission intensity as a function of temperature, depicted in the inset of Figure 21b, was used to calculate TQ$_{1/2}$ and E$_a$ values, which were equal to 291 $\pm$19 K and 0.049 $\pm$0.007 eV, respectively. TQ$_{1/2}$ value is found to be extremely low – emission loses its half efficiency at room temperature.

Moreover, two-exponential PL decay curve at 500 K fades away quicker compared to the one obtained at 77 K (Figure 21c). The data presented in Figure 20d and Table S18 (Appendix 3) indicate that temperature quenching affects the average PL lifetime values of GdPO$_4$:50%Eu^{3+} phosphors as they decrease from ca. 0.87 ms to ca. 0.26 ms with the temperature increase from 77 to 500 K.

Naturally, GdPO$_4$: 50% Eu^{3+} phosphor cannot be considered as a material with high thermal emission stability.
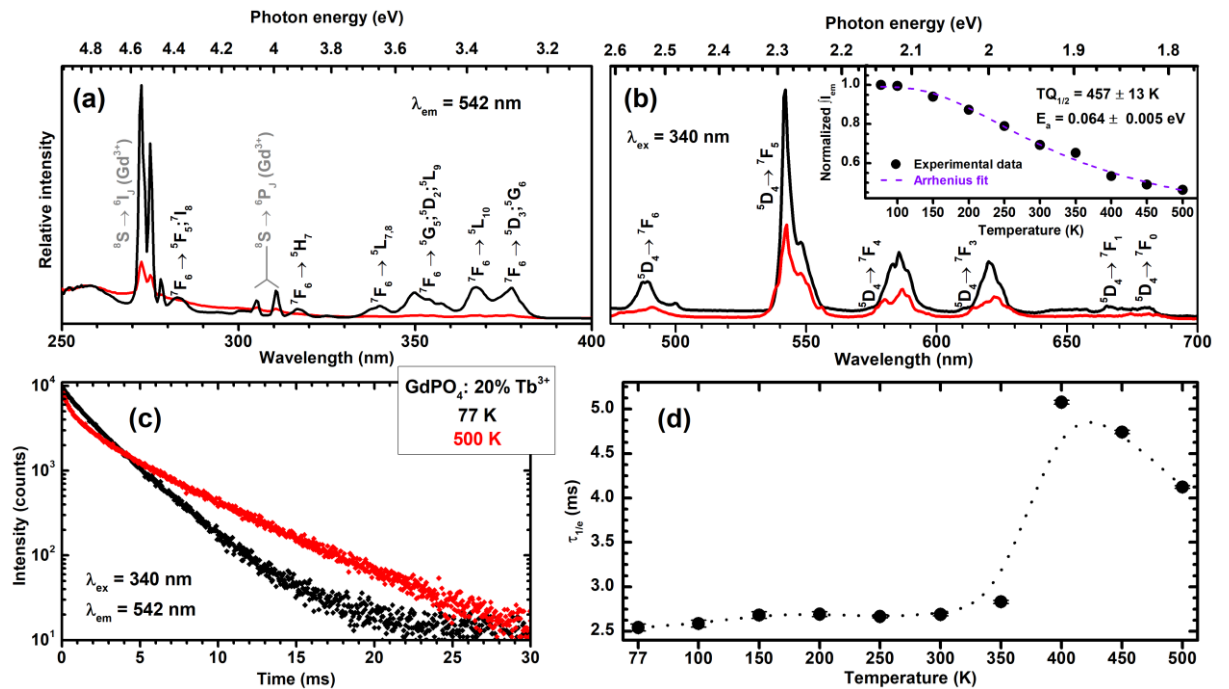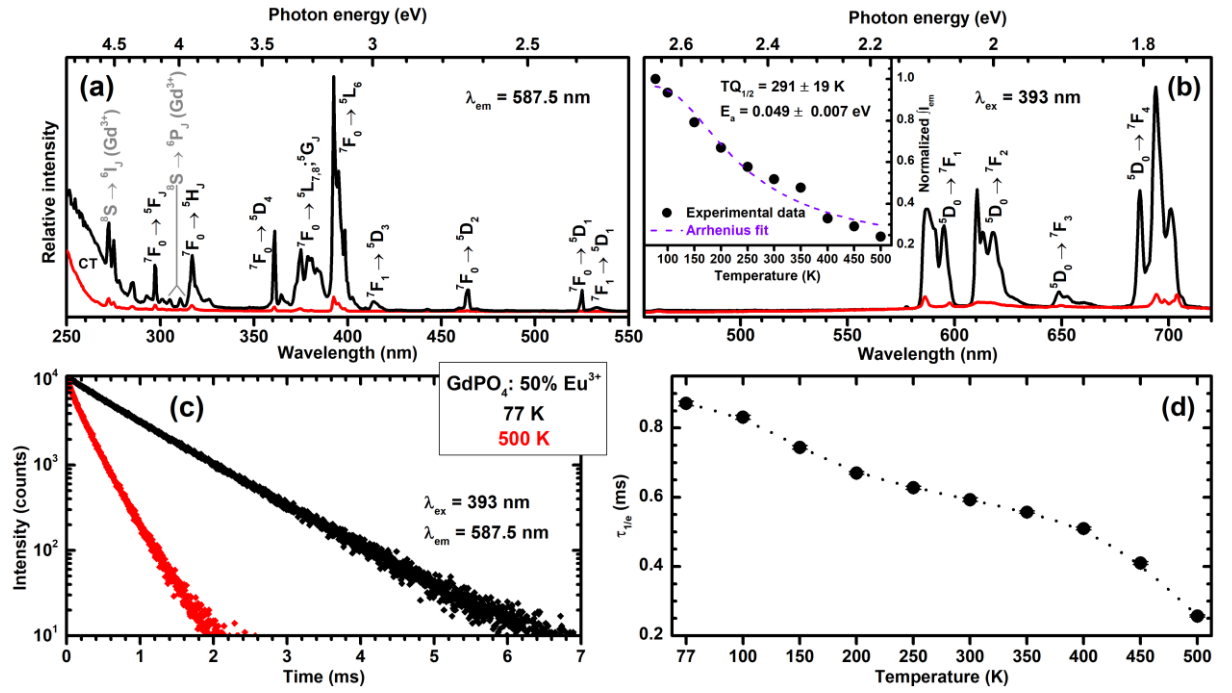
Figure 21. Temperature-dependent excitation (a) and emission (b) spectra with normalized integrated emission intensity as a function of temperature (inset); temperature-dependent PL decay curves (c) and average $\tau_{1/e}$ values as a function of temperature (d) of GdPO$_4$:50%Eu^{3+} phosphor.

3.4   Structural properties of GdPO$_4$ particles doped with different combinations of lanthanide ions

3.4.1   XRD measurements of GdPO$_4$ samples doped with different combinations of lanthanide ions

XRD patterns of each GdPO$_4$ sample doped with different combinations of Ce^{3+}, Tb^{3+} or Eu^{3+} match well with the reference pattern, suggesting that once again the produced particles possess trigonal crystal structure with no impurity phases present (see Figure 22). As expected, these results meet Vegard's law even if 90% of Gd^{3+} in the matrix is replaced by the investigated lanthanide ions (the case of GdPO$_4$:20%Ce^{3+},20%Tb^{3+},50%Eu^{3+} sample).
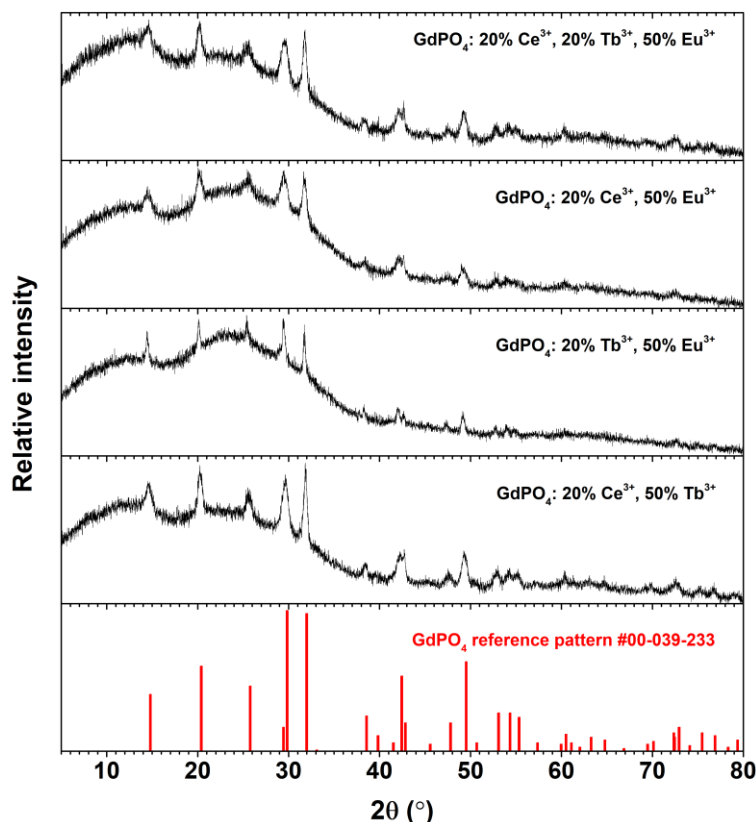
Figure 22. XRD patterns of GdPO$_4$ samples doped with different combinations of Ln^{3+}.

3.4.2 SEM images of GdPO$_4$:20%Ce^{3+},x%Tb^{3+} particles

SEM images of GdPO$_4$:20%Ce^{3+},x%Tb^{3+} nanorods are demonstrated in Figure 23. The calculated average particle size values are presented in Table S8 (see Appendix 2). The average length of GdPO$_4$:20%Ce^{3+},x%Tb^{3+} nanorods slightly increases from ca. 49 nm to ca. 58 nm as the concentration of Tb^{3+} increases from 1% to 50%, respectively. The average width of these particles slightly increases as well and changes from ca. 12 nm to ca. 17 nm as the concentration of Tb^{3+} increases from 1% to 50%, respectively. Since 20% of Ce^{3+} were introduced into the crystal lattice of GdPO$_4$, it is not surprising, that the obtained nanorods are shorter if compared to undoped GdPO$_4$, which average length was ca. 81 nm. However, the width does not change significantly with incorporated dopant ions.
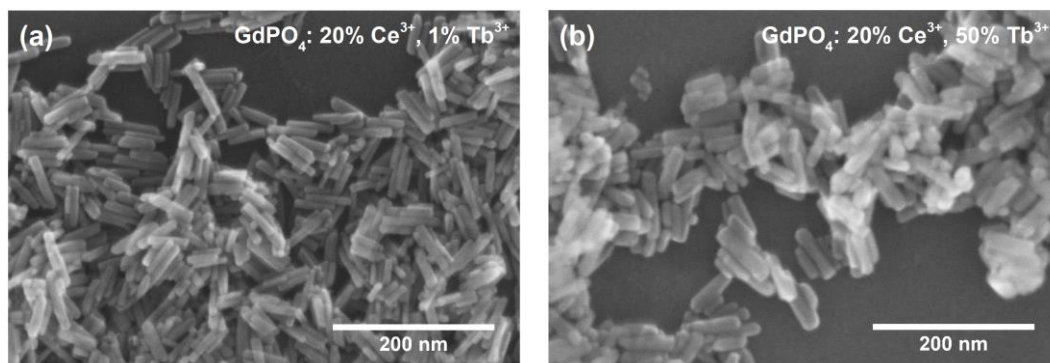
Figure 23. SEM images of GdPO$_4$:20%Ce^{3+},x%Tb^{3+} samples: x = 1 (a) and x = 50 (b).

3.4.3 SEM images of GdPO$_4$:20%Tb^{3+},x%Eu^{3+} particles

SEM images of GdPO$_4$:20%Tb^{3+},x%Eu^{3+} nanorods are demonstrated in Figure 24. The calculated average particle size values are presented in Table S9 (see Appendix 2). The average length of these nanorods significantly decrease from ca. 92 nm to ca. 54 nm as the Eu^{3+} concentration in the sample increased from 1% to 50%, respectively. On the other hand, the average width of the particles increased from ca. 20 nm to ca. 28 nm as the Eu^{3+} concentration in the phosphate increased from 1% to 50%, respectively. As presented in previous chapters, neither Tb^{3+}, nor Eu^{3+} doped GdPO$_4$ NPs showed such significant deviations in the dimensions of obtained nanorods. Unfortunately, no proper explanation of such growth behavior of GdPO$_4$:20%Tb^{3+},x%Eu^{3+} nanorods could be given at the moment.
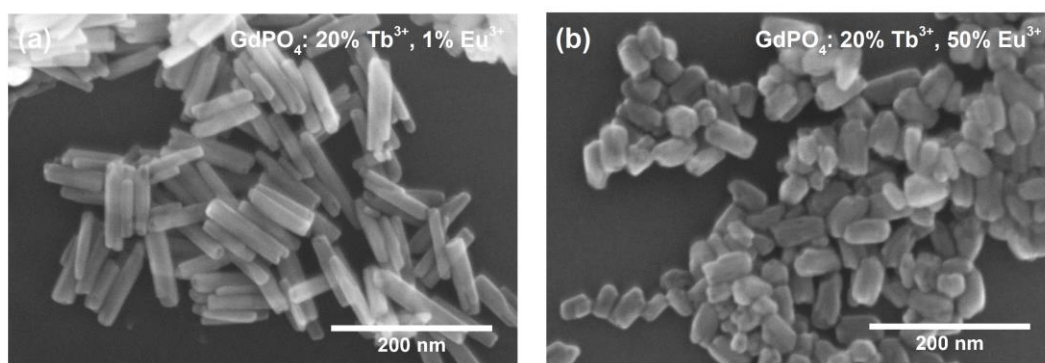
Figure 24. SEM images of GdPO$_4$:20%Tb^{3+},x%Eu^{3+} samples: x = 1 (a) and x = 50 (b).

3.4.4 SEM images of GdPO$_4$:20%Ce^{3+},x%Eu^{3+} particles

SEM images of GdPO$_4$:20%Ce^{3+},x%Eu^{3+} nanorods are shown in Figure 25. The calculated average particle size values are summarized in Table S10 (see Appendix 2). The average length of GdPO$_4$:20%Ce^{3+},x%Eu^{3+} nanorods decrease from ca. 52 nm to ca. 41 nm as the Eu^{3+} concentration increases from 1% to 50%, respectively. Moreover, the average width of these particles negligibly decreases from ca. 12 nm to ca. 10 nm following the same trend. On the other hand, these dimensional changes are within the limits of standard deviation values indicating that the length and width of GdPO$_4$:20%Ce^{3+},x%Eu^{3+} nanorods are barely influenced by the Eu^{3+} concentration. It is also worth mentioning that GdPO$_4$:20%Ce^{3+},x%Eu^{3+} NPs are shorter and thinner if compared to undoped GdPO$_4$ NPs, which are ca. 81 nm in length and ca. 17 nm in width.
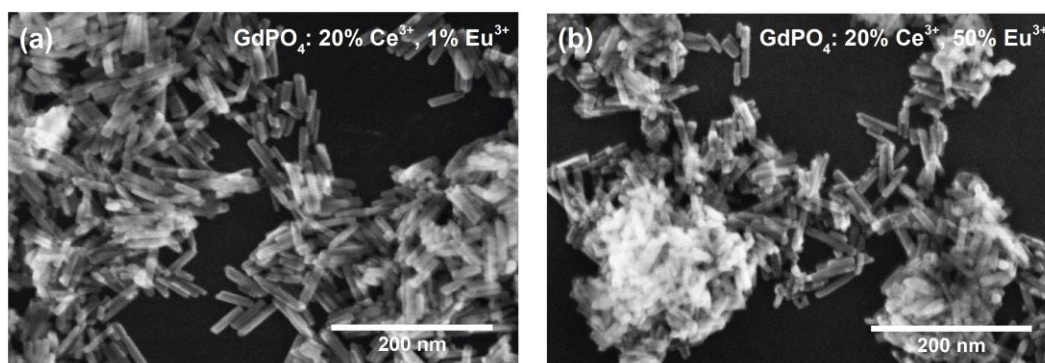
Figure 25. SEM images of GdPO$_4$:20%Ce^{3+},x%Eu^{3+} samples: x = 1 (a) and x = 50 (b).

3.4.5 SEM images of GdPO$_4$:20%Ce^{3+},20%Tb^{3+},x%Eu^{3+} particles

SEM images of GdPO$_4$:20%Ce^{3+},20%Tb^{3+},x%Eu^{3+} nanorods are demonstrated in Figure 26, and the calculated average particle size values are given in Table S11 (see Appendix 2). With increasing Eu^{3+} concentration the dimensions of obtained particles remain virtually the same, i.e., within the limits of their standard deviation values (length decreases from ca. 52 nm to ca.51 nm, and width decreases from ca. 12 nm to ca. 11 nm as the Eu^{3+} concentration increases from 1% to 50%, respectively). As all three chosen lanthanide ions are introduced into the GdPO$_4$ crystal lattice, the obtained nanorods are shorter and thinner if compared to undoped GdPO$_4$.
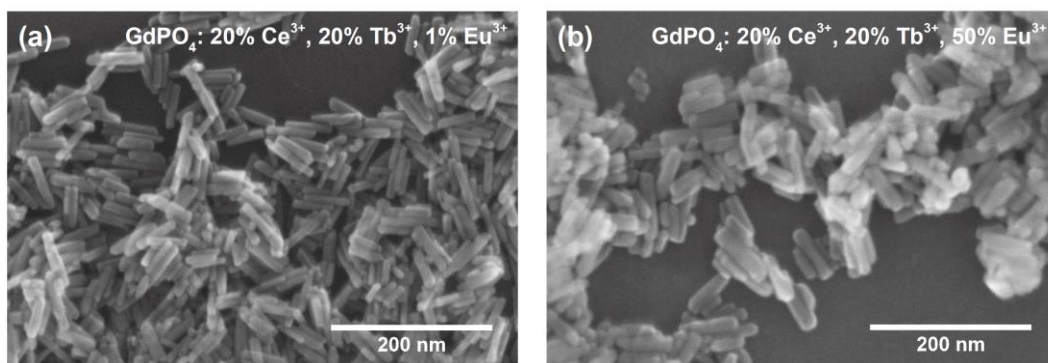
Figure 26. SEM images of GdPO$_4$:20%Ce^{3+},20%Tb^{3+},x%Eu^{3+} samples: x = 1 (a) and x = 50 (b).

3.5 Optical properties of GdPO$_4$ particles doped with different combinations of lanthanide ions

3.5.1 Excitation and emission spectra of GdPO$_4$:20%Ce^{3+},x%Tb^{3+} samples

The excitation and emission spectra of GdPO$_4$:20%Ce^{3+},x%Tb^{3+} phosphors contain typical optical transitions of Ce^{3+} and Tb^{3+} (see Figures 27a and 27b). Excitation spectra are dominated by $^7F_{5/2} \rightarrow$ 5d optical transition of Ce^{3+}, whereas Tb^{3+} excitation lines are barely visible. On the contrary, Ce^{3+} emission is overconcured by the Tb^{3+} optical transitions in the green spectral range (the highest emission intensity was observed at 542 nm originating from $^5D_4 \rightarrow {}^7F_5$ transition).

Figure 27c depicts normalized integrated emission intensity of both Ce^{3+} and Tb^{3+} in the range of 290 – 450 nm and 460 – 700 nm, respectively, as a function of Tb^{3+} concentration in the sample. The given data helps to acknowledge the Ce$^{3+} \rightarrow$ Tb^{3+} energy transfer. As the concentration of Tb^{3+} increases, the emission intensity of Ce^{3+} ions decreases. At the same time the intensity of Tb^{3+} increases until Tb^{3+} concentration reaches 20%. This shows that Ce^{3+} is an excellent sensitizer for Tb^{3+} and this enables excitation of Tb^{3+} in spectral ranges where it normally does not absorb. The substantial emission intensity drop of GdPO$_4$:20%Ce^{3+},50%Tb^{3+} sample is associated with the concentration quenching as was also observed in GdPO$_4$:Tb^{3+} phosphors.
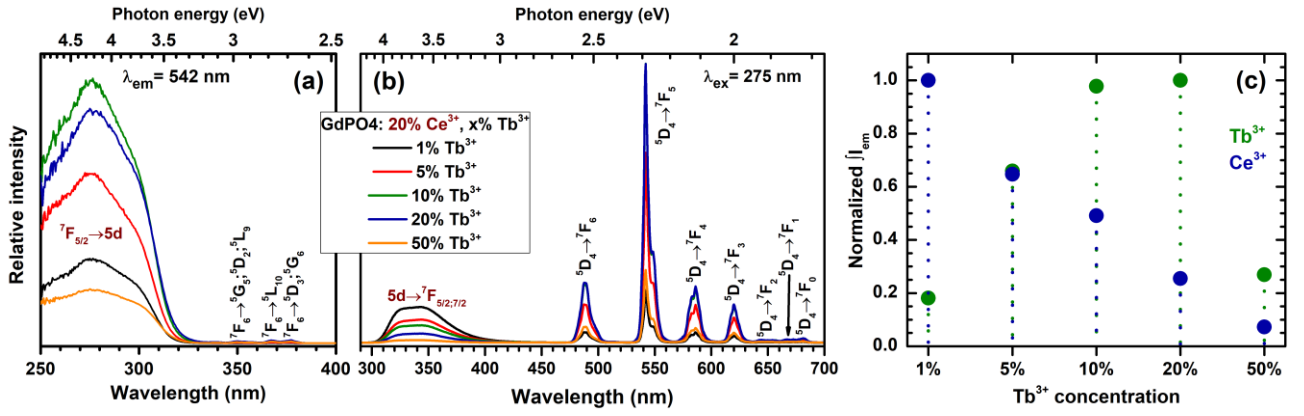
Figure 27. Excitation (a) and emission (b) spectra of GdPO$_4$:20%Ce^{3+},x%Tb^{3+} samples; normalized integrated emission intensity of Ce^{3+} and Tb^{3+} as a function of Tb^{3+} concentration (c).

3.5.2 PL decay of GdPO$_4$:20%Ce^{3+},x%Tb^{3+} samples

Triexponential PL decay of Ce^{3+} (λ_{ex} = 275 nm, λ_{em} = 350 nm) was observed in all GdPO$_4$:20%Ce^{3+},x%Tb^{3+} phosphor samples (see Figure 28). The average PL lifetime values of Ce^{3+} (refer to the inset of Figure 28 and Table S19 in Appendix 3) decrease from ca. 128 ns to ca. 1 ns as the concentration of Tb^{3+} ions increases from 1% to 50%, respectively. Having this data, it is possible to calculate the Ce^{3+} → Tb^{3+} energy transfer efficiency [57]:

$$ET\ efficiency\ (\%) = \left(1 - \frac{\tau_S}{\tau_{S_0}}\right) \times 100\% \qquad (Eq.\ 5)$$

where τ_S is the average PL lifetime value of sensitizer ions in the presence of activator ions, and τ_{S0} is the average PL lifetime value of sensitizer ions in the absence of activator ions.

The obtained ET efficiency values are depicted in the inset of Figure 28 and tabulated in Table S26 (see Appendix 4). The lowest ET efficiency value, only 4%, was obtained for GdPO$_4$:20%Ce^{3+},1%Tb^{3+} sample. In this case, however, it is not surprising since statistically Ce^{3+} and Tb^{3+} are far away from each other. The ET efficiency depends on the sensitizer-activator distance with inverse 6th-power law due to dipole-dipole coupling mechanism [40]. The Ce^{3+} → Tb^{3+} ET efficiency steadily increased with increasing Tb^{3+} concentration and reached 99% for the GdPO$_4$:20%Ce^{3+},50%Tb^{3+} sample.
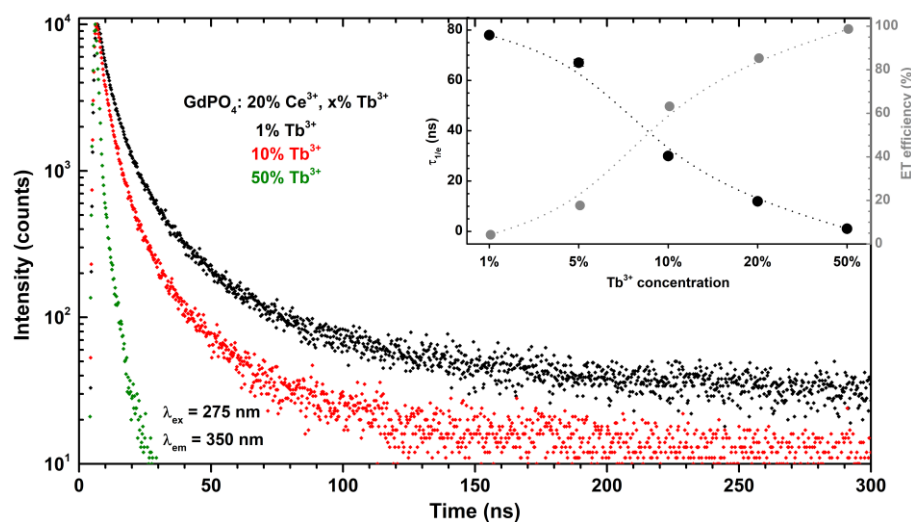
Figure 28. PL decay curves of GdPO$_4$:20%Ce^{3+},x%Tb^{3+} particles; average PL $\tau_{1/e}$ values and ET efficiency as a function of Tb^{3+} concentration (inset).

3.5.3 Thermal impact on optical characteristics of GdPO$_4$:20%Ce^{3+},20%Tb^{3+} samples

Figure 29 shows temperature-dependent optical characteristics (excitation and emission spectra, PL decay curves, average $\tau_{1/e}$ and ET efficiency values) of GdPO$_4$:20%Ce^{3+},20%Tb^{3+} phosphor. It is evident that the intensity of both excitation and emission spectra drops as the temperature rises from 77 to 500 K. Figure 29b shows that Ce^{3+} emission is more temperature sensitive if compared to Tb^{3+}. At 500 K the Ce^{3+} emission completely vanishes whereas ca. 20% of Tb^{3+} emission still remains.

The normalized integrated emission intensity as a function of temperature is shown in the inset of Figure 29b and was used to calculate TQ$_{1/2}$ and E$_a$ values of GdPO$_4$:20%Ce^{3+},20%Tb^{3+} phosphor, which were equal to 434 ±23 K and 0.115 ±0.027 eV, respectively. If compared to the GdPO$_4$:20%Ce^{3+} sample, the addition of Tb^{3+} into this system increased the TQ$_{1/2}$ and E$_a$ values.

Tri-exponential PL decay curve of Ce^{3+} fades away faster with increasing temperature (see Figure 29c). The average PL lifetime values decreased from ca. 2.09 ns to ca. 0.43 ns as the temperature of the sample increased from 77 to 500 K.

The calculated Ce$^{3+} \rightarrow$ Tb^{3+} ET efficiency values (see Table S27, Appendix 4) of GdPO$_4$:20%Ce^{3+},20%Tb^{3+} sample are almost the same (ca. 75%) up to 350 K and then sharply fall with further temperature increase. However, such a phenomenon requires some additional measurements to be completely understood.

Figure 29. Temperature-dependent excitation (a) and emission (b) spectra with normalized integrated emission intensity as a function of temperature (inset); temperature dependent PL decay curves (c) and the average $\tau_{1/e}$ values as well as the ET efficiency values as a function of temperature (d) of GdPO$_4$:20%Ce^{3+},20%Tb^{3+} phosphor.

3.5.4 Excitation and emission spectra of GdPO$_4$:20%Tb^{3+},x%Eu^{3+} samples

The excitation and emission spectra of GdPO$_4$:20% Tb^{3+},x%Eu^{3+} phosphors consist of typical Tb^{3+} and Eu^{3+} optical transitions (see Figures 30a and 30b). In addition, the excitation spectra contain already discussed optical transitions of Gd^{3+}.

Figure 30c depicts the normalized integrated emission intensity of both Tb^{3+} and Eu^{3+} in the range of 450 – 570 nm and 640 – 720 nm, respectively, as a function of Eu^{3+} concentration in the sample. As the concentration of Eu^{3+} increases, the emission intensity of Tb^{3+} steadily decreases (except for GdPO$_4$:20%Tb^{3+},20%Eu^{3+} sample). However, the change of the Eu^{3+} emission intensity showed no continuous trend.

Figure 30. Excitation (a) and emission (b) spectra of GdPO$_4$:20%Tb^{3+},x%Eu^{3+} samples; normalized integrated emission intensity as a function of Eu^{3+} concentration (c).

3.5.5 PL decay of GdPO$_4$:20%Tb^{3+},x%Eu^{3+} samples

All GdPO$_4$:20%Tb^{3+},x% Eu^{3+} phosphor samples demonstrated triexponential PL (λ_{ex} = 486 nm, λ_{em} = 542 nm) decay behavior of Tb^{3+} (see Figure 31). The average $\tau_{1/e}$ values are depicted in the inset of Figure 31 and summarized in Table S21 (see Appendix 3). They are scattered in the range of 0.84 ms $\leq \tau_{1/e} \leq$ ca. 1.90 ms with no uniform trend as the Eu^{3+} concentration increases from 0.5% to 50%.

The calculated ET efficiency values are depicted in the inset of Figure 31. Their exact values are tabulated in Table S28 (see Appendix 4). Since the average PL lifetime values of Tb^{3+} showed no clear trend, the same was observed for ET efficiency values which were scattered in the range from 31% to 70%.
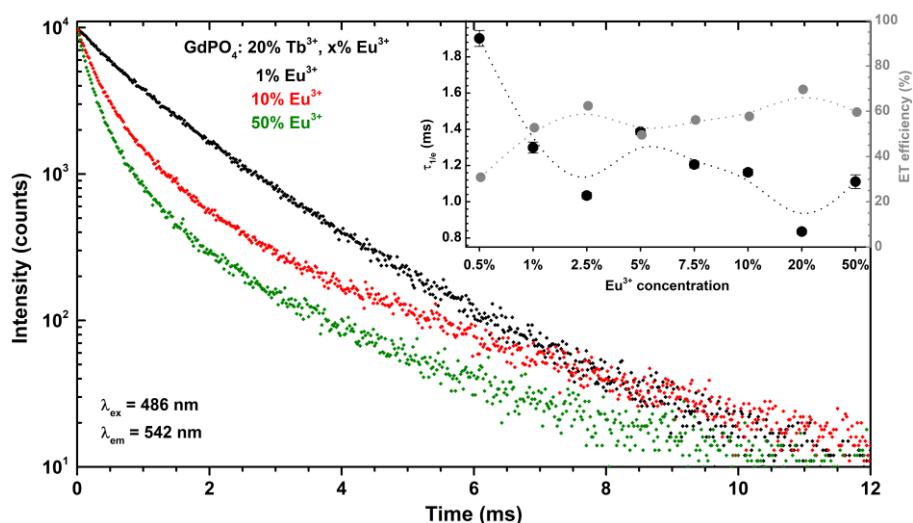
Figure 31. PL decay curves of GdPO$_4$:20%Tb^{3+},x%Eu^{3+} particles; the average $\tau_{1/e}$ values and ET efficiency as a function of Eu^{3+} concentration (inset).

3.5.6 Thermal impact on optical characteristics of GdPO$_4$:20%Tb^{3+},10%Eu^{3+} samples

Figure 32 shows temperature-dependent optical characteristics (excitation and emission spectra, PL decay curves, the average $\tau_{1/e}$ and ET efficiency values) of GdPO$_4$:20%Tb^{3+},10%Eu^{3+} phosphor. The intensity of both excitation and emission spectra drops as the temperature rises from 77 to 500 K.

The normalized integrated emission intensity as a function of temperature is shown in the inset of Figure 32b and was used to calculate TQ$_{1/2}$ and E$_a$ values of GdPO$_4$:20%Tb^{3+},10%Eu^{3+} phosphor, which were equal to 291 $\pm$14 K and 0.033 $\pm$0.003 eV, respectively. Compared to the GdPO$_4$:20%Tb^{3+} sample, the addition of Eu^{3+} to this system has resulted in decreased TQ$_{1/2}$ and E$_a$ values.

Figure 32c shows that tri-exponential PL decay curve fades away faster with the increasing temperature. The calculated average temperature-dependent PL lifetime values are scattered in the range from ca. 1.19 ms to ca. 0.22 ms without a clear trend (see Figure 32d). The exact calculated average $\tau_{1/e}$ values are presented in Table S22 (see Appendix 3). Since the average $\tau_{1/e}$ values showed no clear trend the same was observed with the ET efficiency values (refer to the Table S29 (Appendix 4) for exact values), which were scattered in the 55% $-$ 95% range.
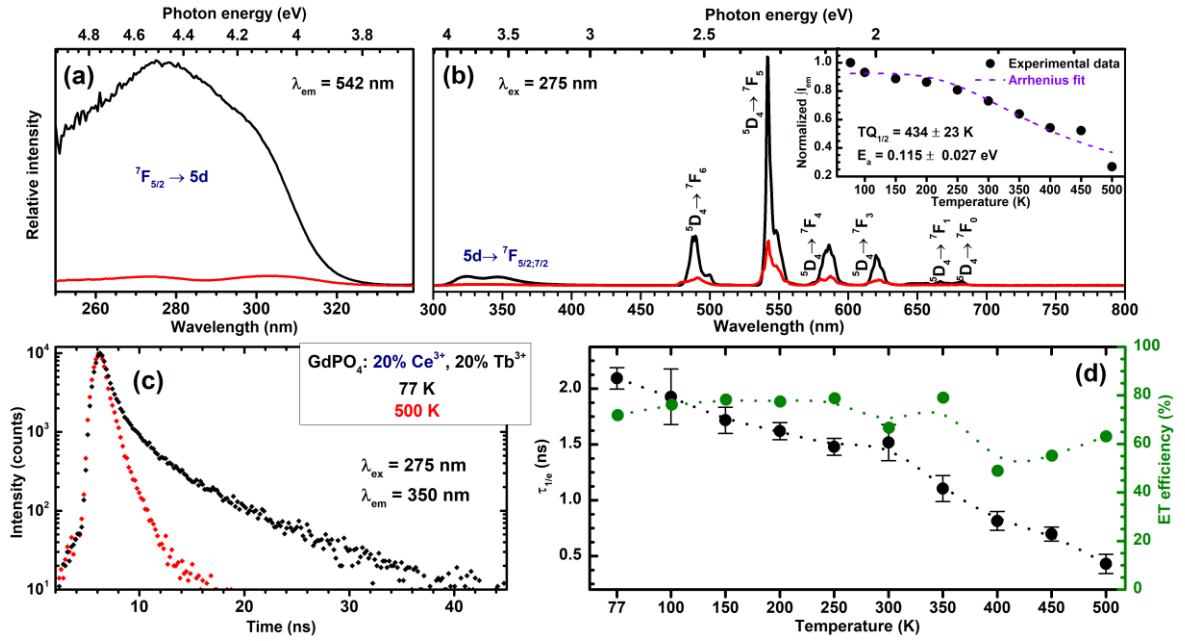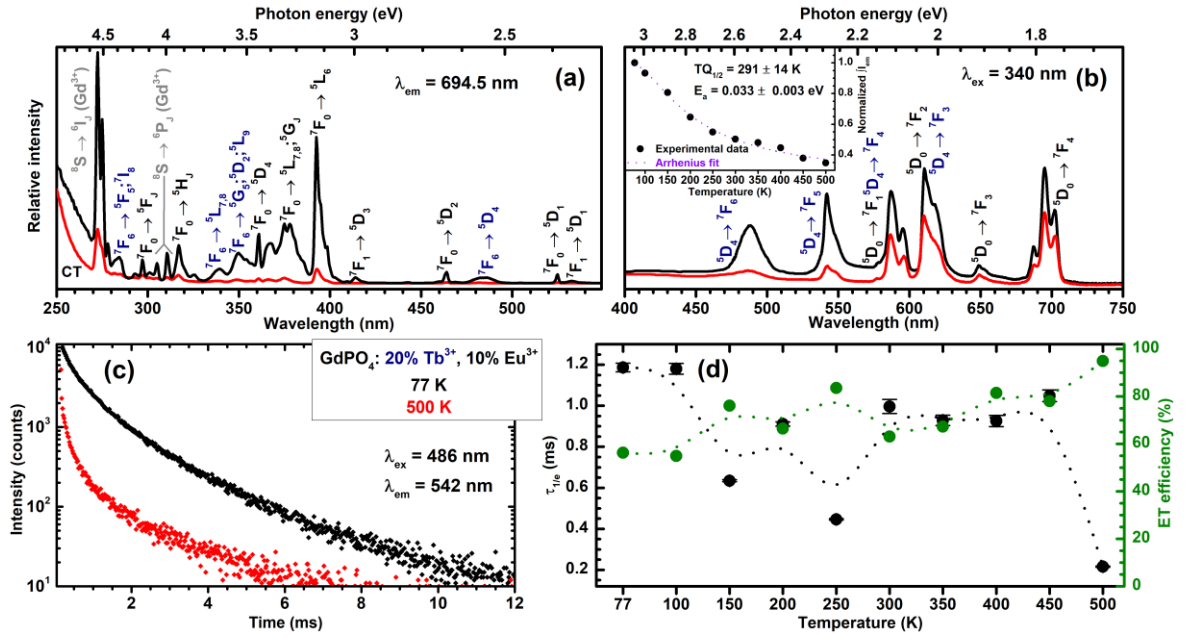
Figure 32. Temperature-dependent excitation (a) and emission (b) spectra with normalized integrated emission intensity as a function of temperature (inset); temperature dependent PL decay curves (c) and the average $\tau_{1/e}$ values as well as the ET efficiency values as a function of temperature (d) of GdPO$_4$:20%Tb^{3+},10%Eu^{3+} phosphor.

3.5.7 Excitation and emission spectra of GdPO$_4$:20%Ce^{3+},x%Eu^{3+} samples

Figure 33 shows excitation and emission spectra in regard with changing the Eu^{3+} concentration in GdPO$_4$:20%Ce^{3+},x%Eu^{3+} samples. Both excitation and emission spectra contain the already discussed optical transitions of Ce^{3+} and Eu^{3+}. Unfortunately, the addition of Eu^{3+} decreases the integrated emission intensity (see Figure 33c) of both Ce^{3+} (290 – 450 nm range) and Eu^{3+} (570 – 720 nm) until the amount of Eu^{3+} in NPs reaches 10%. Further increase of Eu^{3+} concentration leads to an increase of emission intensities.
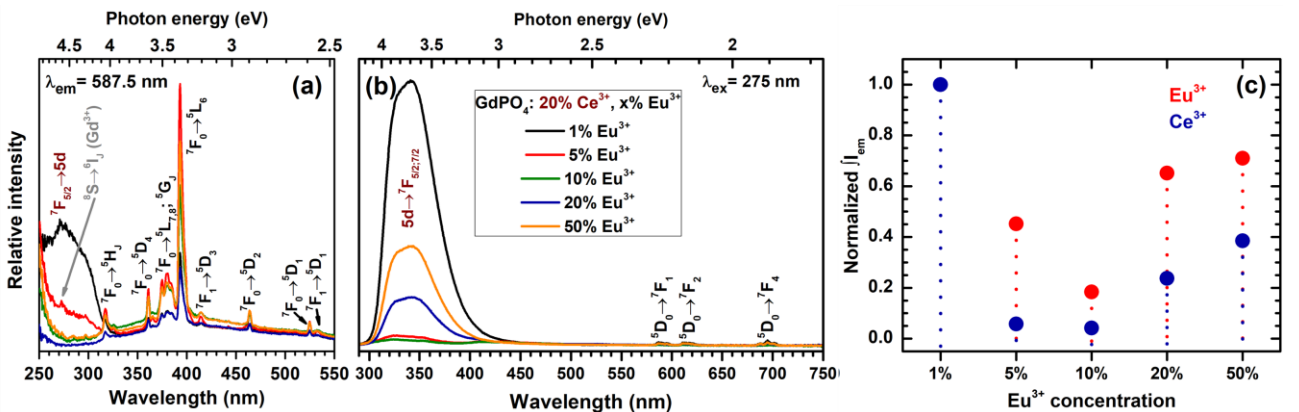
Figure 33. Excitation (a) and emission (b) spectra of GdPO$_4$:20%Ce^{3+},x%Eu^{3+} samples; normalized integrated emission intensity as a function of Eu^{3+} concentration (c).

3.5.8 PL decay of GdPO$_4$:20% Ce^{3+},x%Eu^{3+} samples

Triexponential PL decay of Ce^{3+} ions was observed in all GdPO$_4$:20%Ce^{3+},x%Eu^{3+} phosphor samples (see Figure 34). The average PL lifetime values (see inset of Figure 34, and Table S23 in Appendix 3) drastically decrease from ca. 10.63 ns to ca. 0.93 ns as the Eu^{3+} concentration increases from 0.5% to 50%, respectively.

The calculated ET efficiency values are depicted in the inset of Figure 34 and the exact values are tabulated in Table S30 (see Appendix 4). The ET efficiency values increased from 87% for GdPO$_4$:20%Ce^{3+},0.5%Eu^{3+} sample to 99% for GdPO$_4$:20%Ce^{3+},50%Eu^{3+} sample. However, these values should be taken with caution since the already mentioned charge transfer (Ce^{3+} + Eu^{3+} ↔ Ce^{4+} + Eu^{2+}) between Ce^{3+} and Eu^{3+} can significantly reduce the PL lifetime of Ce^{3+}. The charge transfer is a competitive process to the energy transfer and is responsible for the emission quenching in Ce^{3+} −Eu^{3+} system [63].
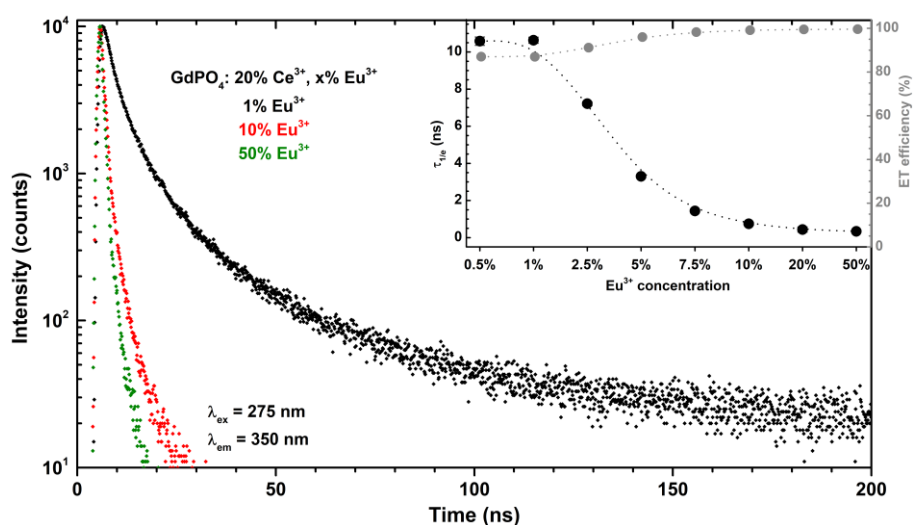
Figure 34. PL decay curves of GdPO$_4$:20%Ce^{3+},x%Eu^{3+} particles; the average $\tau_{1/e}$ values and ET efficiency as a function of Eu^{3+} concentration (inset).

3.5.9 Excitation and emission spectra of GdPO$_4$:20%Ce^{3+},20%Tb^{3+},x%Eu^{3+} samples

Excitation and emission spectra of GdPO$_4$:20%Ce^{3+},20%Tb^{3+},x%Eu^{3+} samples are shown in Figure 35a and Figure 35b, respectively. They consist of the already discussed typical optical transitions of Ce^{3+}, Tb^{3+}, and Eu^{3+}. The excitation spectra are dominated by Ce^{3+} $^7F_{5/2}$ → 5d optical transition, while emission spectra are dominated by Tb^{3+} optical transitions ($^5D_4$ → $^7F_{3,4,5,6}$). However, as the Eu^{3+} concentration increases, both excitation and emission peaks of Ce^{3+}, Tb^{3+}, and Eu^{3+} become barely noticeable. In addition, the emission intensity of either dopant ions drops exponentially as the Eu^{3+} concentration increases from 1% to 50% (see Figure 35c). Such a phenomenon is established due to Ce^{3+} → Eu^{3+} electron (charge) transfer, which quenches optical transitions of these ions. Even though the excitation wavelength is chosen to meet the energy levels of Ce^{3+}, Tb^{3+} can not be effectively excited through Ce^{3+} → Tb^{3+} ET, since with increasing Eu^{3+} concentration electron (charge) transfer between Ce^{3+} and Eu^{3+} becomes a more dominant process and less Ce^{3+} can transfer energy to Tb^{3+}.
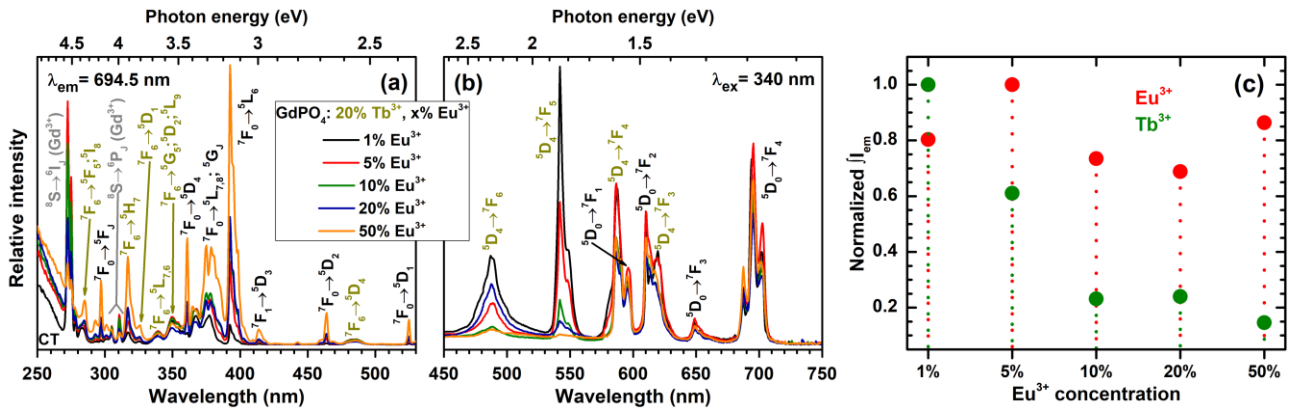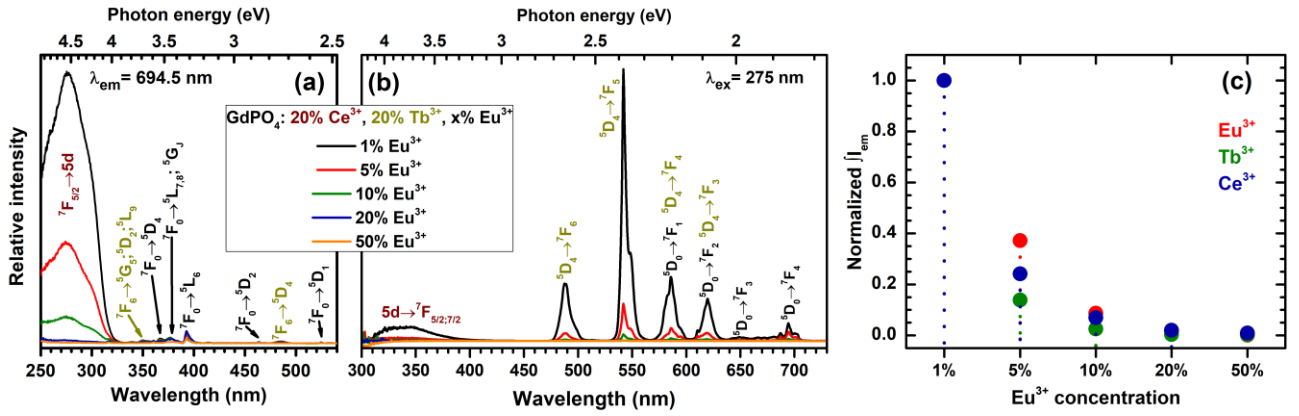
Figure 35. Excitation (a) and emission (b) spectra of GdPO$_4$:20%Ce^{3+},20%Tb^{3+},x%Eu^{3+} samples; normalized integrated emission intensity as a function of Eu^{3+} concentration (c).

3.5.10 PL decay of GdPO$_4$:20%Ce^{3+},20%Tb^{3+},x%Eu^{3+} samples

Triexponential PL decay of Ce^{3+} ions (λ_{ex} = 275 nm, λ_{em} = 350 nm) was observed in all GdPO$_4$:20%Ce^{3+},20%Tb^{3+},x%Eu^{3+} phosphor samples (see Figure 36). The calculated average $\tau_{1/e}$ values are shown in the inset of Figure 36 and tabulated in Table S24 (see Appendix 3). It is evident that the average $\tau_{1/e}$ values drastically decrease from ca. 3.22 ns to ca. 0.38 ns as the Eu^{3+} concentration increases from 0.5% to 50%, respectively, and are much shorter if compared to the GdPO$_4$:20%Ce^{3+},x%Eu^{3+} samples.

The calculated ET efficiency values are depicted in the inset of Figure 36 and summarized in Table S31 (see Appendix 4). The ET efficiency values increased from 96% for GdPO$_4$:20%Ce^{3+},20%Tb^{3+},0.5%Eu^{3+} sample to 99% for GdPO$_4$:20%Ce^{3+},20%Tb^{3+},50%Eu^{3+} sample. As seen in the case of GdPO$_4$:20%Ce^{3+},x%Eu^{3+} samples, these calculated ET values should be taken with caution as they also include the electron (charge) transfer (Ce^{3+} + Eu^{3+} $\leftrightarrow$ Ce^{4+} + Eu^{2+}) efficiency as well.
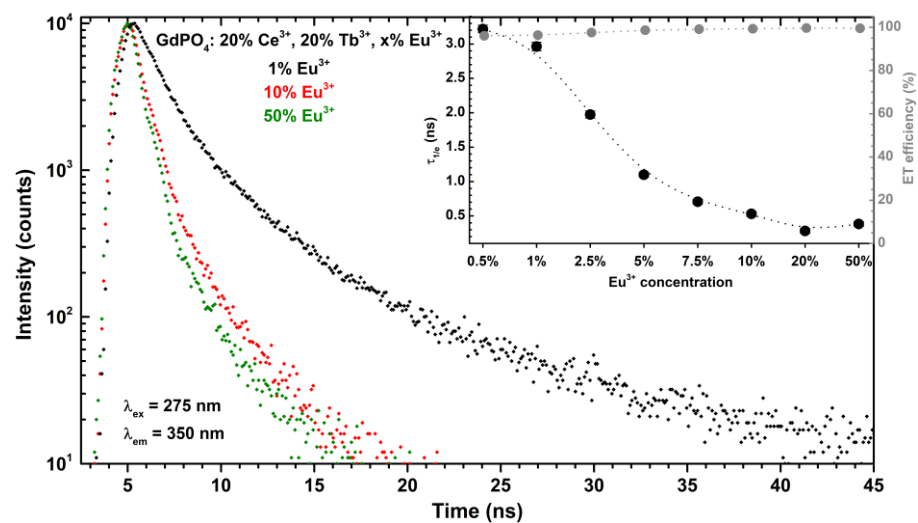
Figure 36. PL decay curves of GdPO$_4$:20%Ce^{3+},20%Tb^{3+},x%Eu^{3+} particles; the average PL $\tau_{1/e}$ values and ET efficiency as a function of Eu^{3+} concentration (inset).

3.6 Investigation of GdPO$_4$:15%Eu^{3+} particles as a multimodal bioimaging agent

3.6.1 Structural and morphological properties of GdPO$_4$:15%Eu^{3+} particles

XRD patterns of the produced GdPO$_4$:15%Eu^{3+} samples match well with the reference pattern (Figure 37a), indicating that phase pure particles with trigonal crystal structure were obtained under any <Gd> : <P> molar ratio chosen. Furthermore, as the <Gd> : <P> molar ratio increases the broader the peaks of XRD patterns were recorded, which indicates that smaller particles form when smaller amounts of phosphate precursor are used. Such peak broadening is caused because periodic atomic arrangements that generate the sharp diffraction peak profile are limited as the particles measured are of nanoscale dimensions [61]. Broad diffraction band from 5° to approx. 35° is observed due to the amorphous glass substrate used during measurements.

The morphology and particle size distribution of the prepared phosphates were determined via the detailed analysis of their SEM images (see Figures 37b-d). SEM images of the synthesized GdPO$_4$:15%Eu^{3+} samples reveal that decreasing <Gd>:<P> molar ratio in the order of 1:10, 1:50, and 1:100, nanorods, nanoprisms and sub-microspheres were obtained, respectively. SEM images were also used for the calculations of size distribution of GdPO$_4$:15% Eu^{3+} particles and the obtained results are depicted in Figures 37e-g, which show that dimensions of nanorods are of higher monodispersity if compared to nanoprisms or sub-microspheres. It can also be deduced that the width values of either GdPO$_4$:15%Eu^{3+} nanorods or nanoprisms are less scattered than the ones of length. Moreover, the calculated average nanorod width and length were 15 and 73 nm, respectively, and average nanoprism width and length were 57 and 94 nm. The average width of sub-microspheres was 117 nm. In addition, it is worth mentioning that both nanoprisms and sub-microspheres seem to consist of nanorods stacked side by side. This trend was also observed in the previous research conducted by our group as well and was explained by the preferred trigonal phase growth along the *c*-axis, the orientation of which coincides with the zeolitic channels containing crystalline water [3].
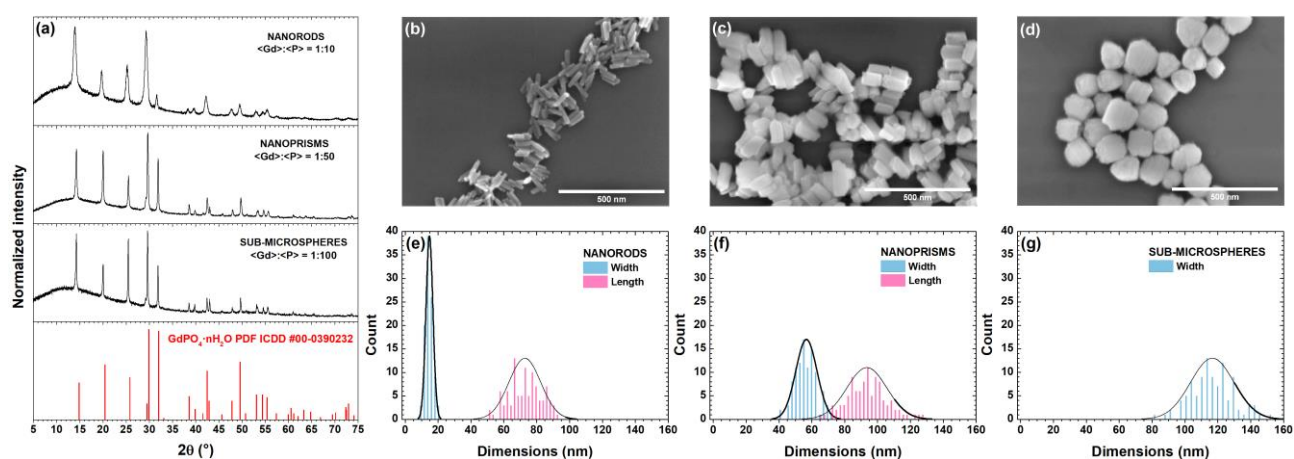
Figure 37. XRD patterns of GdPO$_4$:15%Eu^{3+} particles with different morphology and GdPO$_4$·nH$_2$O reference pattern (a). SEM images of GdPO$_4$:15%Eu^{3+} nanorods (b), nanoprisms (c) and sub-microspheres (d), and illustrations of their size distribution (e, f, and g, respectively).

3.6.2 Optical properties of GdPO$_4$:15%Eu^{3+} particles

Excitation spectra of the synthesized GdPO$_4$:15%Eu^{3+} particles (see Figure 38a) consist of typical Eu^{3+} optical transitions as well as a ligand to metal charge transfer (CT) band (O^{2-} → Eu^{3+}). A couple of excitation lines of Gd^{3+} optical transitions were also observed indicating the presence of Gd^{3+} → Eu^{3+} energy transfer. The highest intensity excitation line at 393 nm is attributed to the $^7F_0$ → $^5L_6$ optical transition of Eu^{3+}. Emission peaks observed (see Figure 38b) comply with Eu^{3+} energy level scheme and the highest intensity emission line at ca. 695 nm is assigned to the $^5D_0$ → $^7F_4$ optical transition of Eu^{3+}. The highest overall emission intensity was observed for GdPO$_4$:15%Eu^{3+} sub-micro spheres, followed by nanoprisms, and nanorods, respectively. This can be explained when the results of BET surface area measurements are considered. The surface area of nanorods is the largest and equal to 41.46 m^2/g, following the surface area of nanoprisms – 19.31 m^2/g, and the smallest surface area was the one for sub-microspheres – 11.49 m^2/g. Sub-microspheres possess the smallest surface area; therefore, their emission is less quenched since less surface defects are introduced into the crystal structure of these particles in comparison with nanoprisms or nanorods [40, 44].

Figure 38c illustrates the recorded emission decay curves (λ_{ex} = 393 nm, λ_{em} = 586 nm). In each case two-exponential PL decay was observed, which could be described by Equation 4. The average PL lifetime values were virtually identical regardless the morphology of produced particles: 1.06 ± 0.01 ms, 1.03 ± 0.02 ms and 1.09 ± 0.02 ms for nanorods, nanoprisms and sub-microspheres, respectively.

The emission spectra were also used to calculate color coordinates of the produced compounds. Figure 38 shows the CIE 1931 color space diagram with GdPO$_4$:15%Eu^{3+} color coordinates which are in the orange-red spectral region. Moreover, the human eye would perceive the GdPO$_4$:15%Eu^{3+} emission as a monochromatic light since all the color coordinates are located directly on the edge of the CIE 1931 color space diagram (i.e., sample emission possess high color purity) [32].
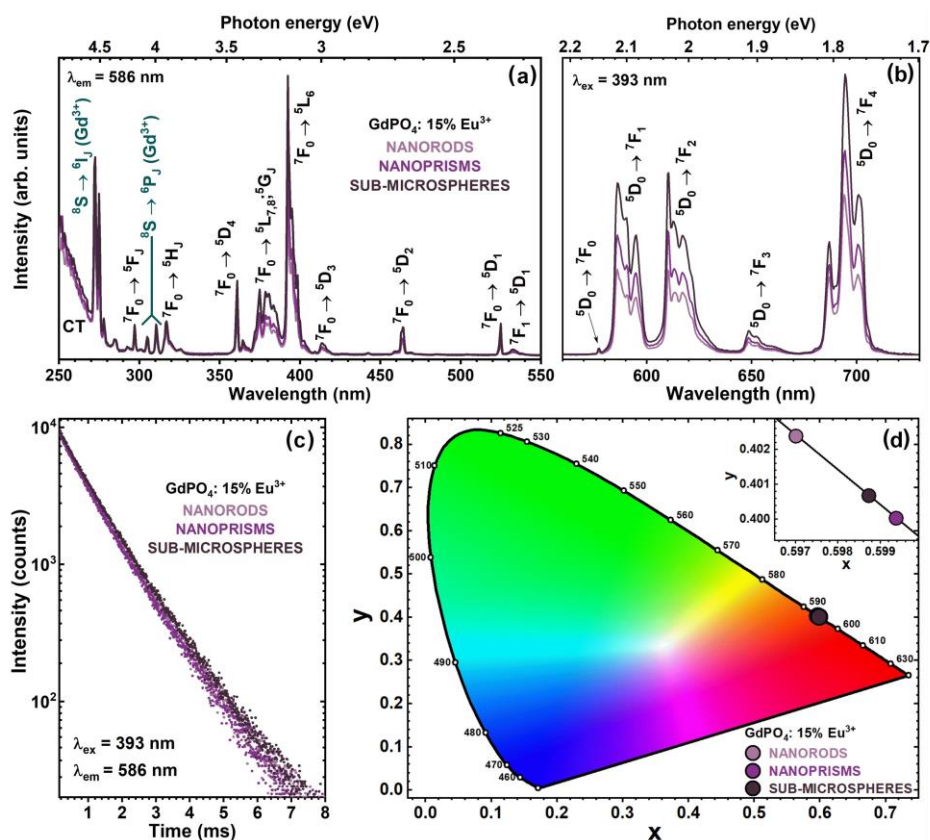
Figure 38. Emission (a) and excitation (b) spectra, PL decay curves (c) and CIE 1931 color space diagram showing color coordinates of GdPO$_4$: 15% Eu^{3+} particles with different morphology (d).

3.6.3 Initial investigation of GdPO$_4$:15%Eu^{3+} particles' biocompatibility and potential as bioimaging agent

Zooplankton *Daphnia Magna* (image on the left hand side of Figure 39) are primary and one of the most commonly used model species in standardized ecotoxicity and nanotoxicology tests; therefore, it was chosen for the initial biocompatibility investigation of GdPO$_4$:15%Eu^{3+} NPs [64]. The advantages of using zooplankton *Daphnia Magna* include a short generation time, small body sizes, and the ability to produce large populations rapidly. The change in the heart rate, as an index of the toxic effects on *Daphnia Magna*, is in most cases used in acute toxicity tests [65].

Table 2 shows the mortality results (24 h experiment) of *Daphnia Magna* exposed to different types of GdPO$_4$:15%Eu^{3+} NPs. The LC$_{50}$ value was found to be the lowest for nanorods (52 μg/mL) and *Daphnia Magna* sensitivity to NPs varies depending on their type as follows: nanorods > nanoprisms > sub-microspheres.

Table 2. Comparison of LC$_{50}$ values of *Daphnia Magna* exposed to nanoprisms, nanorods, and sub-microspheres of GdPO$_4$:15%Eu^{3+}.

GdPO$_4$:15%Eu^{3+} morphology	LC$_{50}$, μg/mL
Nanorods	52.36
Nanoprisms	60.15
Sub-microspheres	64.47

On the right-hand side of Figure 39, a representative confocoal microscopy image of a single *Daphnia Magna* with the red-emitting $GdPO_4$:15%Eu^{3+} nanorods visible in its digestive tract is presented. The initial tests show that the amount of zooplankton's consumed phosphate NPs decreases in such order: nanorods > nanoprisms > sub-microspheres. These results are not suprising, since nanorods are the smallest if compared to other tested morphologies of $GdPO_4$:15%Eu^{3+}.

Hereafter, the three morphologies of $GdPO_4$:15%Eu^{3+} phosphor are being further tested as a biomarker and a potential MRI agent. The results of this reasearch will be released in a publication in colaboration with the National Cancer Institute.

Figure 39. Optical microscopy image of a single *Daphnia Magna* (left) and representative confocoal microscopy image of a single *Daphnia Magna* with $GdPO_4$:15%Eu^{3+} nanorods visible in its digestive tract (right).

CONCLUSIONS

1. $GdPO_4$ nanorods with the highest monodispersity (length equal to 81 ±9 nm, width equal to 17 ±3 nm) were obtained via hydrothermal synthesis method under molar ratio <Gd> : <P> = 1:10, and pH = 10.

2.   Phase pure trigonal $GdPO_4$ and $GdPO_4$: Ln^{3+} (Ln^{3+} = Ce^{3+}, Tb^{3+}, Eu^{3+}) samples were produced as was verified by powder XRD measurements.

3.   Spectroscopic analysis of single lanthanide ion (Ce^{3+}, Tb^{3+}, or Eu^{3+}) doped $GdPO_4$ NPs revealed that:

- the highest emission intensity was registered for $GdPO_4$:5%Ce^{3+}, $GdPO_4$:20%Tb^{3+}, and $GdPO_4$:50%Eu^{3+} phosphors with peak emission intensities at 344 nm (NUV), 542 nm (green), and 694.5 nm (red), respectively;
- none of the produced samples showed high thermal emission stability (the highest $TQ_{1/2}$ = 457 ±13 K belongs to $GdPO_4$:20%Tb^{3+}).

4.   Spectroscopic analysis of $GdPO_4$ NPs doped with various combinations of Ce^{3+}, Tb^{3+}, and Eu^{3+} demonstrated that:

- with increasing Tb^{3+} amount in the $GdPO_4$:20%Ce^{3+},x%Tb^{3+} NPs the ET efficiency values increase as well (the highest ET efficiency value belongs to 50% Tb^{3+} doped phosphor and is equal to 99%);
- with increasing Eu^{3+} amount in the $GdPO_4$:20%Tb^{3+},x%Eu^{3+} NPs the ET efficiency values scatter in the range from 31% to 70%;
- the emission of $GdPO_4$:20%Ce^{3+},x%Eu^{3+} and $GdPO_4$:20%Ce^{3+},20%Tb^{3+},x%Eu^{3+} NPs was strongly quenched due to CT between Ce^{3+} and Eu^{3+};
- none of the produced samples showed high thermal emission stability (the highest $TQ_{1/2}$ = 434 ±23 K was obtained for $GdPO_4$:20%Ce^{3+},20%Tb^{3+}).

5. $GdPO_4$:15% Eu^{3+} samples with the sub-microsphere morphology showed the highest overall emission intensity as well as the lowest toxicity to *Daphnia Magna* species if compared to other morphologies of NPs tested.

All in all, Ce^{3+}/Tb^{3+}, or Tb^{3+}/Eu^{3+} pair doped $GdPO_4$ NPs might be considered as a potential anti-counterfeit agents and singly Eu^{3+}, or Tb^{3+}/Eu^{3+} pair doped phosphors show valid prospects as multimodal biomimaging materials.

REFERENCES

1. Wang, G., Q. Peng, and Y. Li, *Lanthanide-doped nanocrystals: synthesis, optical-magnetic properties, and applications.* Accounts of chemical research, 2011. **44**(5): p. 322-332.
2. Zhou, J., et al., *Upconversion luminescent materials: advances and applications.* Chemical reviews, 2015. **115**(1): p. 395-465.
3. Janulevicius, M., et al., *Controlled hydrothermal synthesis, morphological design and colloidal stability of $GdPO_4 \cdot nH_2O$ particles.* Materials Today Communications, 2020. **23**: p. 100934.
4. Sun, X., et al., *Sol–gel syntheses, luminescence, and energy transfer properties of α-GdB_5O_9:Ce^{3+}/Tb^{3+} phosphors.* Dalton Transactions, 2015. **44**(5): p. 2276-2284.
5. Baur, F., F. Glocker, and T. Jüstel, *Photoluminescence and energy transfer rates and efficiencies in Eu^{3+} activated $Tb_2Mo_3O_{12}$.* Journal of Materials Chemistry C, 2015. **3**(9): p. 2054-2064.
6. Ochiai, A. and S. Utsunomiya, *Crystal chemistry and stability of hydrated rare-earth phosphates formed at room temperature.* Minerals, 2017. **7**(5): p. 84.
7. Ni, Y., J.M. Hughes, and A.N. Mariano, *Crystal chemistry of the monazite and xenotime structures.* American Mineralogist, 1995. **80**(1-2): p. 21-26.
8. Janulevičius, M., *Engineering of lanthanide orthophosphate functional nanomaterials.* 2020, Vilniaus universitetas.
9. Assaaoudi, H., A. Ennaciri, and A. Rulmont, *Vibrational spectra of hydrated rare earth orthophosphates.* Vibrational Spectroscopy, 2001. **25**(1): p. 81-90.
10. Mesbah, A., et al., *In pursuit of the rhabdophane crystal structure: from the hydrated monoclinic $LnPO_4$:0.667 H_2O to the hexagonal $LnPO_4$ (Ln= Nd, Sm, Gd, Eu and Dy).* Journal of Solid State Chemistry, 2017. **249**: p. 221-227.
11. Mesbah, A., et al., *Monoclinic form of the rhabdophane compounds: $REEPO_4 \cdot 0.667H_2O$.* Crystal growth & design, 2014. **14**(10): p. 5090-5098.
12. Buissette, V., et al., *Colloidal Synthesis of Luminescent Rhabdophane $LaPO_4$:Ln^{3+} xH_2O (Ln= Ce, Tb, Eu; $x \approx 0.7$) Nanocrystals.* Chemistry of materials, 2004. **16**(19): p. 3767-3773.
13. Shannon, R.D., *Revised effective ionic radii and systematic studies of interatomic distances in halides and chalcogenides.* Acta crystallographica section A: crystal physics, diffraction, theoretical and general crystallography, 1976. **32**(5): p. 751-767.
14. Kizilyalli, M. and A. Welch, *Crystal data for lanthanide orthophosphates.* Journal of Applied Crystallography, 1976. **9**(5): p. 413-414.
15. Byrappa, K. and M. Yoshimura, *Handbook of hydrothermal technology.* 2012: William Andrew.
16. Feng, S.-H. and G.-H. Li, *Hydrothermal and solvothermal syntheses*, in *Modern inorganic synthetic chemistry.* 2017, Elsevier. p. 73-104.
17. Paglione, J., N.P. Butch, and E.E. Rodriguez, *Fundamentals of Quantum Materials: A Practical Guide to Synthesis and Exploration.* 2021: World Scientific.
18. Cao, Y., et al., *Sol-precipitation-hydrothermal synthesis and luminescence of $GdPO_4$:Tb^{3+} submicron cubes.* Chemical Physics Letters, 2016. **651**: p. 80-83.
19. Song, H., et al., *Hydrothermal synthesis, characterization and luminescent properties of $GdPO_4 \cdot H_2O$:Tb^{3+} nanorods and nanobundles.* Materials Research Bulletin, 2013. **48**(12): p. 5013-5018.
20. Yang, R., et al., *Redox hydrothermal synthesis of cerium phosphate microspheres with different architectures.* CrystEngComm, 2011. **13**(24): p. 7284-7292.
21. Zhang, X., et al., *Hydrothermal synthesis and luminescent properties of $LaPO_4$:Eu 3D microstructures with controllable phase and morphology.* Materials Research Bulletin, 2010. **45**(9): p. 1324-1329.
22. Ma, L., et al., *Hydrothermal growth and morphology evolution of $CePO_4$ aggregates by a complexing method.* Materials Research Bulletin, 2008. **43**(11): p. 2840-2849.

23. Feng, S. and R. Xu, *New materials in hydrothermal synthesis.* Accounts of chemical research, 2001. **34**(3): p. 239-247.

24. Bosze, E.J., et al., *Improving the efficiency of a blue-emitting phosphor by an energy transfer from Gd^{3+} to Ce^{3+}.* Journal of Luminescence, 2003. **104**(1): p. 47-54.

25. Blasse, G., *Chapter 34 Chemistry and physics of R-activated phosphors*, in *Handbook on the Physics and Chemistry of Rare Earths*. 1979, Elsevier. p. 237-274.

26. Sytsma, J., W. van Schaik, and G. Blasse, *Vibronic transitions in the emission spectra of Gd^{3+} in several rare-earth compounds.* Journal of Physics and Chemistry of Solids, 1991. **52**(2): p. 419-429.

27. Li, J.-G. and Y. Sakka, *Recent progress in advanced optical materials based on gadolinium aluminate garnet ($Gd_3Al_5O_{12}$).* Science and Technology of Advanced Materials, 2015.

28. Tamrakar, R.K., et al., *Ytterbium doped gadolinium oxide (Gd_2O_3: Yb^{3+}) phosphor: topology, morphology, and luminescence behaviour.* Indian Journal of Materials Science, 2014. **2014**.

29. Matos, M.G., et al., *Synthesis and luminescent properties of gadolinium aluminates phosphors.* Inorganica Chimica Acta, 2011. **375**(1): p. 63-69.

30. Maldiney, T., et al., *Gadolinium-doped persistent nanophosphors as versatile tool for multimodal in vivo imaging.* Advanced Functional Materials, 2015. **25**(2): p. 331-338.

31. Mahakhode, J.G., A. Nande, and S.J. Dhoble, *A review: X-ray excited luminescence of gadolinium based optoelectronic phosphors.* Luminescence, 2021. **36**(6): p. 1344-1353.

32. Yen, W.M. and H. Yamamoto, *Fundamentals of phosphors.* 2018: CRC press.

33. Yen, W., et al., *Luminescence and photoconductivity of cerium compounds.* Acta Physica Polonica-Series A General Physics, 1996. **90**(2): p. 257-266.

34. Katelnikovas, A., et al., *Efficient cerium-based sol–gel derived phosphors in different garnet matrices for light-emitting diodes.* Journal of alloys and compounds, 2011. **509**(21): p. 6247-6251.

35. Katelnikovas, A., *Synthesis and characterization of luminescent materials for solid state light sources.* 2012.

36. Xia, Z. and A. Meijerink, *Ce^{3+}-Doped garnet phosphors: composition modification, luminescence properties and applications.* Chemical Society Reviews, 2017. **46**(1): p. 275-299.

37. Herrmann, A., et al., *Spectroscopic properties of cerium-doped aluminosilicate glasses.* Optical Materials Express, 2015. **5**(4): p. 720-732.

38. Verstegen, J., J.L. Sommerdijk, and J. Verriet, *Cerium and terbium luminescence in $LaMgAl_{11}O_{19}$.* Journal of Luminescence, 1973. **6**(5): p. 425-431.

39. Binnemans, K., *Interpretation of europium (III) spectra.* Coordination Chemistry Reviews, 2015. **295**: p. 1-45.

40. Shionoya, S., W.M. Yen, and H. Yamamoto, *Phosphor handbook.* 2018: CRC press.

41. Innocenzi, V., et al., *A hydrometallurgical process for the recovery of terbium from fluorescent lamps: experimental design, optimization of acid leaching process and process analysis.* Journal of environmental management, 2016. **184**: p. 552-559.

42. Xia, F., et al., *Fast and intense green emission of Tb^{3+} in borosilicate glass modified by Cu^+.* Scientific Reports, 2015. **5**(1): p. 1-7.

43. Nakahara, Y., et al., *Fluorescent silica nanoparticles modified chemically with terbium complexes as potential bioimaging probes: their fluorescence and colloidal properties in water.* New Journal of Chemistry, 2015. **39**(2): p. 1452-1458.

44. Blasse, G. and B.C. Grabmaier, *Luminescent Materials.* 2012: Springer Berlin Heidelberg.

45. Hänninen, P. and H. Härmä, *Lanthanide luminescence: photophysical, analytical and biological aspects.* Vol. 7. 2011: Springer Science & Business Media.

46. Radkov, E.V., et al., *Red emitting phosphor materials for use in LED and LCD applications.* 2008, Google Patents.

47. Sun, C., et al., *Synthesis and radioluminescence of PEGylated Eu^{3+}-doped nanophosphors as bioimaging probes.* Advanced materials, 2011. **23**(24): p. H195-H199.

48.   Blasse, G., H.S. Kiliaan, and A.J. De Vries, *A study of the energy transfer processes in sensitized gadolinium phosphors.* Journal of the Less Common Metals, 1986. **126**: p. 139-146.

49.   Zhang, X., et al., *Luminescence of $SrGdGa_3O_7:RE^{3+}$ (RE=Eu, Tb) phosphors and energy transfer from Gd3+ to RE3+.* Materials Research Bulletin, 2005. **40**(2): p. 281-288.

50.   Carnall, W., H. Crosswhite, and H.M. Crosswhite, *Energy level structure and transition probabilities in the spectra of the trivalent lanthanides in LaF_3.* 1978, Argonne National Lab.(ANL), Argonne, IL (United States).

51.   Weber, M., *Optical spectra of Ce^{3+} and Ce^{3+}-sensitized fluorescence in $YAlO_3$.* Journal of Applied Physics, 1973. **44**(7): p. 3205-3208.

52.   Huang, C.H. and A. Tsourkas, *Gd-based Macromolecules and Nanoparticles as Magnetic Resonance Contrast Agents for Molecular Imaging.* Current Topics in Medicinal Chemistry, 2013. **13**(4): p. 411-421.

53.   Hifumi, H., et al., *Gadolinium-based hybrid nanoparticles as a positive MR contrast agent.* Journal of the American Chemical Society, 2006. **128**(47): p. 15090-15091.

54.   Kumari, M., S. Mondal, and P.K. Sharma, *Synthesis, characterization and electrochemical monitoring of drug release properties of dual stimuli responsive mesoporous $GdPO_4:Eu^{3+}$ nanoparticles.* Journal of Alloys and Compounds, 2019. **776**: p. 654-665.

55.   Yang, Q.H., et al., *Short-wave near-infrared emissive $GdPO_4: Nd^{3+}$ theranostic probe for in vivo bioimaging beyond 1300 nm.* Rsc Advances, 2018. **8**(23): p. 12832-12840.

56.   Lv, R.C., et al., *Multifunctional $LaPO_4$:Ce/Tb@Au mesoporous microspheres: synthesis, luminescence and controllable light triggered drug release.* Rsc Advances, 2014. **4**(108): p. 63425-63435.

57.   Baur, F., F. Glocker, and T. Jüstel, *Photoluminescence and energy transfer rates and efficiencies in Eu^{3+} activated $Tb_2Mo_3O_{12}$.* Journal of Materials Chemistry C, 2015. **3**(9): p. 2054-2064.

58.   Sulcius, S., et al., *The profound effect of harmful cyanobacterial blooms: From food-web and management perspectives.* Science of the Total Environment, 2017. **609**: p. 1443-1450.

59.   Hamilton, M.A., R.C. Russo, and R.V. Thurston, *Trimmed Spearman-Karber method for estimating median lethal concentrations in toxicity bioassays.* Environmental Science & Technology, 1977. **11**(7): p. 714-719.

60.   Ropp, R.C., *Luminescence and the Solid State.* 2004: Elsevier Science.

61.   Waseda, Y., E. Matsubara, and K. Shinoda, *X-ray diffraction crystallography: introduction, examples and solved problems.* 2011: Springer Science & Business Media.

62.   Jubera, V., et al., *Luminescent properties of Eu^{3+}-activated lithium rare earth borates and oxyborates.* Journal of Luminescence, 2003. **101**(1): p. 1-10.

63.   Yanes, A.C., J. del-Castillo, and E. Ortiz, *Energy transfer and tunable emission in $BaGdF_5:RE^{3+}$ (RE= Ce, Tb, Eu) nano-glass-ceramics.* Journal of Alloys and Compounds, 2019. **773**: p. 1099-1107.

64.   Martinez, D.S.T., et al., *Daphnia magna and mixture toxicity with nanomaterials – Current status and perspectives in data-driven risk prediction.* Nano Today, 2022. **43**: p. 101430.

65.   Lee, S., et al., *Fe(III)-doped activated biochar sorbents trigger mitochondrial dysfunction with oxidative stress on Daphnia magna.* Chemosphere, 2022. **288**: p. 132608.

SUMMARY

VILNIUS UNIVERSITY
FACULTY OF CHEMISTRY AND GEOSCIENCES

Eglė Ežerskytė

Synthesis, Structural and Optical Characteristics of GdPO$_4$: Ln^{3+} (Ln^{3+} = Ce^{3+}, Tb^{3+}, Eu^{3+}) Nanoparticles

This master thesis describes synthesis of GdPO$_4$ NPs doped with lone Ce^{3+}, Tb^{3+}, or Eu^{3+} ions and their various combinations following structural and spectroscopic investigation of the produced samples regarding the evaluation of such phosphors as anti-counterfeit pigments or bioimaging agents.

Hydrothermal synthesis route was chosen to produce all the samples for this research. XRD analysis assured that materials with trigonal crystal structure were synthesized and no phase impurities were detected. SEM images revealed that particles formed were of nanoscale dimensions.

Optical properties of GdPO$_4$ NPs doped with lone Ce^{3+}, Tb^{3+}, or Eu^{3+} ions or their various combinations were examined via recording excitation and emission spectra, PL decay curves and temperature-dependent excitation, emission spectra, and PL decay curves. The obtained measurement data was used to evaluate the efficiency of ET processeses, average PL lifetime values, CIE 1931 color space coordinates, TQ$_{1/2}$ and E$_a$ values of produced phosphors.

GdPO$_4$:Ce^{3+}/Tb^{3+}/Eu^{3+} samples demonstrated a typical emission spectra in near UV, green, and red spectral range, respectively. ET efficiency values of GdPO$_4$:Ce^{3+},Tb^{3+} and GdPO$_4$:Tb^{3+},Eu^{3+} NPs reached up to 99% and 95%, respectively. The emission spectra of phosphates doped with Ce^{3+}/Eu^{3+} pair or Ce^{3+}/Tb^{3+}/Eu^{3+} triplet was strongly quenched due to CT process between Ce^{3+} and Eu^{3+} ions.

The analysis of the obtained results suggests that Ce^{3+}/Tb^{3+}, or Tb^{3+}/Eu^{3+} pair doped GdPO$_4$ phosphors could be further examined as a potential anti-counterfeit pigment and singly Eu^{3+}, or Tb^{3+}/Eu^{3+} pair doped NPs are valid candidates for multimodal bioimaging.

SANTRAUKA

VILNIAUS UNIVERSITETAS
CHEMIJOS IR GEOMOKSLŲ FAKULTETAS

Eglė Ežerskytė
$GdPO_4$: Ln^{3+} (Ln^{3+} = Ce^{3+}, Tb^{3+}, Eu^{3+}) nanodalelių sintezė, struktūrinių ir optinių savybių tyrimas

Šiame magistriniame darbe aprašoma $GdPO_4$ nanodalelių, legiruotų pavieniais Ce^{3+}, Tb^{3+} arba Eu^{3+} jonais bei įvairiomis šių jonų kombinacijomis, sintezė, struktūrinė bei spektroskopinė analizė. Tyrimo metu buvo siekiama įvertinti, ar šios liuminescencinės medžiagos galėtų būti panaudojamos kaip vertingų daiktų saugos pigmentai arba žymekliai biovaizdinime.

Visi baigiamajame darbe analizuoti mėginiai buvo susintetinti hidroterminiu metodu. Trigoninės kristalinės struktūros dalelių fazinis grynumas buvo patvirtintas XRD metodu. SEM nuotraukos parodė, kad visų susintetintų liuminoforų dalelių matmenys yra nano eilės.

Optinės $GdPO_4$ nanodalelių, legiruotų pavieniais Ce^{3+}, Tb^{3+} arba Eu^{3+} jonais bei įvairiomis šių jonų kombinacijomis, savybės buvo įvertintos užrašant mėginių sužadinimo ir emisijos spektrus, liuminescencijos gesimo kreives kambario temperatūroje, bei sužadinimo, emisijos spektrus bei gesimo kreives 77 – 500 K temperatūrų intervale. Matavimų duomenys buvo panaudoti energijos pernašos procesų, vidutinių emisijos gesimo trukmės verčių, CIE 1931 spalvinių koordinačių, $TQ_{1/2}$ ir E_a verčių nustatymui.

Sužadintos $GdPO_4$:Ce^{3+}/Tb^{3+}/Eu^{3+} nanodalelės atitinkamai spinduliavo artimojo ultravioleto, žalioje ir raudonoje spektro srityse. $GdPO_4$:Ce^{3+},Tb^{3+} junginių serijos energijos pernašos našumo vertės siekė net 99 %, o $GdPO_4$:Tb^{3+},Eu^{3+} junginių serijos atveju – 95 %. Dėl krūvio pernašos tarp Ce^{3+} ir Eu^{3+} jonų, fosfatų, legiruotų Ce^{3+} ir Eu^{3+} jonų pora ar Ce^{3+}, Tb^{3+} ir Eu^{3+} jonų kombinacijomis, emisija buvo stipriai gesinama.

Tyrimo rezultatai parodė, kad $GdPO_4$:Ce^{3+}/Tb^{3+} ir $GdPO_4$:Tb^{3+}/Eu^{3+} junginiai galėtų būti toliau analizuojami kaip potencialūs saugos pigmentai, o $GdPO_4$:Eu^{3+}/Tb^{3+} ir $GdPO_4$:Eu^{3+} nanodalelės yra potencialios kaip biovaizdinimo žymenys.

LIST OF PUBLICATIONS AND CONFERENCE ATTENDANCE

List of publications

1. Grigorjevaite, J., **Ezerskyte, E.**, Minderyte, A., Stanionyte, S., Juskenas, R., Sakirzanovas, S. and Katelnikovas, A., 2019. Optical properties of red-emitting $Rb_2Bi(PO_4)(MoO_4):Eu^{3+}$ powders and ceramics with high quantum efficiency for white LEDs. Materials, 12(19), p.3275.

2. **Ezerskyte, E.**, Grigorjevaite, J., Minderyte, A., Saitzek, S. and Katelnikovas, A., 2020. Temperature-dependent luminescence of red-emitting $Ba_2Y_5B_5O_{17}:Eu^{3+}$ phosphors with efficiencies close to unity for near-UV LEDs. Materials, 13(3), p.763.

3. Grigorjevaite, J., Janulevicius, M., Kruopyte, A., **Ezerskyte, E.**, Vargalis, R., Sakirzanovas, S. and Katelnikovas, A., 2020. Synthesis and optical properties of efficient orange emitting $GdB_5O_9:Sm^{3+}$ phosphors. Journal of Sol-Gel Science and Technology, 94(1), pp.80-87.

4. Grigorjevaite, J., **Ezerskyte, E.**, Páterek, J., Saitzek, S., Zabiliūtė-Karaliūnė, A., Vitta, P., Enseling, D., Jüstel, T. and Katelnikovas, A., 2020. Luminescence and luminescence quenching of $K_2Bi(PO_4)(MoO_4):Sm^{3+}$ phosphors for horticultural and general lighting applications. Materials Advances, 1(5), pp.1427-1438.

5. Van der Heggen, D., Zilenaite, R., **Ezerskyte, E.**, Fritz, V., Korthout, K., Vandenberghe, D., De Grave, J., Garrevoet, J., Vincze, L., Poelman, D. and Joos, J.J., 2021. A Standalone, Battery-Free Light Dosimeter for Ultraviolet to Infrared Light. Advanced Functional Materials, p.2109635.

List of attended conferences

1. J. Grigorjevaite, **E. Ezerskyte**, L. Mikoliunaite. "Evolution of Light Sources". The International Conference Dedicated to the 215th Birth Anniversary of Ignacy Domeyko. Vilnius, Lithuania, July 28 – 29, (2017).

2. **E. Ezerskyte**, A. Katelnikovas. "Upconversion Luminescence of $Lu_6(W,Mo)O_{12}:Yb^{3+}/Er^{3+}$ Phosphors with Rhombohedral and Cubic Crystal Structure". 61st International Conference Open Readings. Vilnius, Lithuania, March 20 – 23, (2018).

3. **E. Ežerskytė**, A. Katelnikovas. „Aukštynvertės emisijos polimorfiniuose molibdatuose ir volframatuose tyrimas". Studentų moksliniai tyrimai 2017 – 2018 metais. Vilnius, Lietuva, birželio 14 d., (2018).

4. **E. Ezerskyte**, A. Katelnikovas. "Luminescence of $K_2(Cs,Rb)Y(VO_4)_2:Eu^{3+}$ Phosphors with Trigonnal Crystal Structure". 62nd International Conference Open Readings. Vilnius, Lithuania, March 19 – 22, (2019).

5. **E. Ezerskyte**, A. Katelnikovas. "Conventional and Upconversion Luminescence of Polymorphous $BiPO_4:Yb^{3+},Tb^{3+},Eu^{3+}$ Phosphors". 63rd International Conference Open Readings. Vilnius, Lithuania, March 17 – 20, (2020).

6. **E. Ezerskyte**, A. Katelnikovas. "Synthesis and Optical Properties Investigation of Multi-Colour Emitting $GdPO_4:Ce^{3+}/Tb^{3+},Eu^{3+}$ Nanoparticles". 64th International Conference Open Readings. Vilnius, Lithuania, March 16 – 19, (2021).

7. **E. Ežerskytė**, A. Katelnikovas. „Multispalvinių $GdPO_4:Ce^{3+}/Tb^{3+},Eu^{3+}$ liuminescencinių nanodalelių sintezė ir optinių savybių tyrimas". Studentų moksliniai tyrimai 2020 – 2021 metais. Vilnius, Lietuva, gegužės 11 d., (2021).

8. Jonušauskas, L., Andrijec, D., Andriukaitis, D., Vargalis, R., Baravykas, T., Stankevičius, A., Merkininkaite, G., Pautienius, A., Gricius, H., **Ežerskyte, E**. and Šimkutė, E., 2021, March. Expansion of direct laser writing (DLW) capabilities for usage in biomedical applications. In Laser 3D Manufacturing VIII (Vol. 11677, p. 1167713). International Society for Optics and Photonics.

ACKNOWLEDGEMENTS

PADĖKOS

Už pasitikėjimą, suteiktas galimybes, kantrybę ir liuminescencijos pamokas visada liksiu dėkinga savo baigiamojo darbo vadovui prof. dr. Artūrui Katelnikovui. Kaip šiandien atsimenu tą dieną ir džiaugsmą, kai pakvietėte prisijungti prie savo mokslinių tyrimų grupės. AČIŪ!

Ypatingai džiaugiuosi užsimezgusiu bendradarbiavimu su dr. Vaidu Klimkevičiumi. Esu dėkinga už patobulintus praktinio darbo laboratorijoje įgūdžius, įkvepiantį ir motyvuojantį profesinį užsidegimą. Man esi mokslininko pavyzdys!

Atspirtį šio baigiamojo darbo tyrimams suteikė dr. Matas Janulevičius. Ačiū! Be Tavo įdirbio šis tiriamasis darbas būtų keliskart sudėtingesnis.

Prof. dr. Simui Šakirzanovui tariu ačiū už tiriamiesiems darbams suteiktą infrastruktūrą ir raginančius žodžius.

Prof. dr. Vitalijui Karabanovui ir Jo vadovaujamai komandai Nacionaliniame vėžio institute (NVI) dėkoju už tyrimus, siekiant įvertinti realias susintetintų nanodalelių panaudojimo galimybes biomedicinos srityje.

Doktorantėms Julijai Grigorjevaitei ir Gretai Merininkaitei esu dėkinga už lengvo pokalbio minutes tarp darbų.

Už rūpestį ir juoką iki ašarų dėkoju Deividui ir Henrikui.

Rokai, ačiū už nuoširdžius pokalbius, išgertus kavos puodelius ir įgyvendinimo laukiančius planus. Y kāp y, y bi y.

Juzefai, Rugile ir Živile – esate atokvėpis ir neišsenkantis palaikymas šitame vakarėlyje. Tikiuosi vieną dieną pajėgsiu atsilyginti Jums tuo pačiu.

Tėčiui, mamai ir broliui – ačiū, kad su Jumis visada jaučiuosi svarbi ir laukiama. Kasdien stengiuosi ir stengsiuosi, kad galėtumėte didžiuotis savo dukra ir seserimi.

SUPPLEMENTARY MATERIAL

PARAMETERS OF SPECTROSCOPIC MEASUREMENTS

Table S1. Recording parameters of excitation and emission spectra.

GdPO$_4$ samples doped with:	Excitation spectra			Emission spectra		
	λ_{em}, nm	Excitation slit, nm	Emission slit, nm	λ_{ex}, nm	Excitation slit, nm	Emission slit, nm
Ce^{3+}	360.0	0.80	2.00	275.0	2.00	0.80
Tb^{3+}	542.0	0.60	3.50	340.0	3.50	0.60
Eu^{3+}	587.5	0.50	3.50	393.0	3.50	0.50
Ce^{3+}, Tb^{3+}	542.0	0.50	2.00	275.0	3.00	0.75
Tb^{3+}. Eu^{3+}	694.5	1.00	5.00	340.0	3.00	0.75
Ce^{3+}, Eu^{3+}	587.5	2.00	5.00	275.0	5.00	2.00
Ce^{3+}, Tb^{3+}, Eu^{3+}	694.5	2.00	5.00	275.0	5.00	0.75

Table S2. Recording parameters of PL decay curves.

GdPO$_4$ samples doped with:	λ_{em}, nm	λ_{ex}, nm
Ce^{3+}	350.0	275.0
Tb^{3+}	542.0	340.0
Eu^{3+}	587.5	393.0
Ce^{3+}, Tb^{3+}	350.0	275.0
Tb^{3+}. Eu^{3+}	542.0	486.0
Ce^{3+}, Eu^{3+}	350.0	275.0
Ce^{3+}, Tb^{3+}, Eu^{3+}	350.0	275.0

SIZE MEASUREMENTS OF THE PRODUCED PHOSPHATE PARTICLES

Table S3. Average dimensions of produced GdPO$_4$ samples at neutral reaction media (pH = 7) using different <Gd> : <P> molar ratio.

<Gd> : <P> molar ratio	Length, nm	Standard deviation, nm	Width, nm	Standard deviation, nm
1:7.5	154	26	19	3
1:10	135	19	17	3
1:12.5	116	19	23	3
1:15	109	12	19	3
1:17.5	106	13	21	3
1:20	118	13	26	3
1:25	106	10	31	4
1:30	106	14	32	5
1:50	128	19	60	8

Table S4. Average dimensions of produced GdPO$_4$ samples using molar ratio <Gd> : <P> = 1:10 at different pH of the reaction mixture.

pH	Length, nm	Standard deviation, nm	Width, nm	Standard deviation, nm
4	635	107	93	26
5	382	75	41	6
6	230	25	31	4
8	135	14	22	3
9	107	11	20	3
10	81	9	17	3
11	99	13	23	3

Table S5. Average dimensions of produced $GdPO_4$: Ce^{3+} samples.

Ce^{3+} conc.	Length, nm	Standard deviation, nm	Width, nm	Standard deviation, nm
5%	59	17	13	3
10%	56	16	14	3
20%	41	8	12	2
25%	41	9	13	2
50%	29	6	9	1
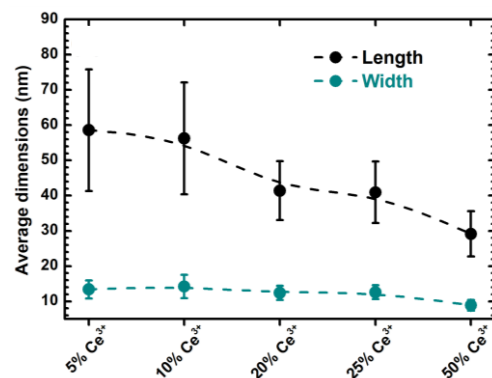
Table S6. Average dimensions of produced $GdPO_4$: Tb^{3+} samples.

Tb^{3+} conc.	Length, nm	Standard deviation, nm	Width, nm	Standard deviation, nm
1%	75	14	19	4
5%	82	12	19	3
10%	83	11	19	3
20%	86	12	22	3
50%	89	15	20	2
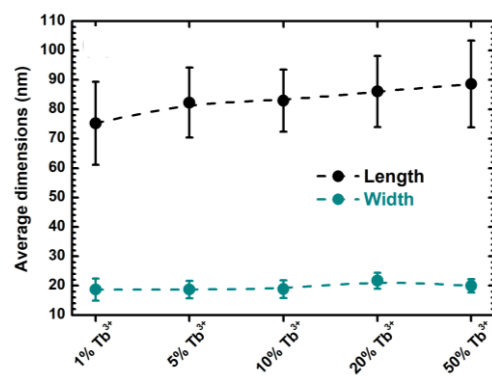
Table S7. Average dimensions of produced $GdPO_4$: Eu^{3+} samples.

Eu^{3+} conc.	Length, nm	Standard deviation, nm	Width, nm	Standard deviation, nm
1%	88	21	21	2
5%	89	17	23	5
10%	85	16	19	3
20%	82	17	18	3
50%	74	10	18	2
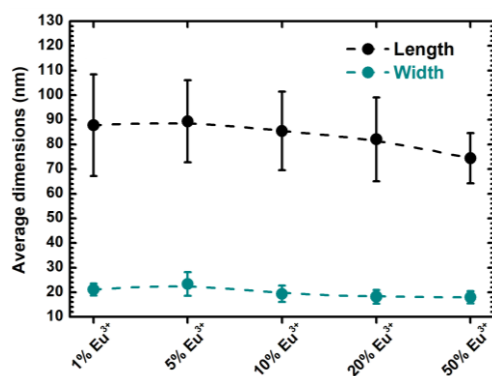
Table S8. Average dimensions of produced GdPO$_4$:20%Ce^{3+},x%Tb^{3+} samples.

Tb^{3+} conc.	Length, nm	Standard deviation, nm	Width, nm	Standard deviation, nm
1%	49	9	12	2
5%	56	9	12	2
10%	56	9	13	2
20%	57	13	14	2
50%	58	12	17	3
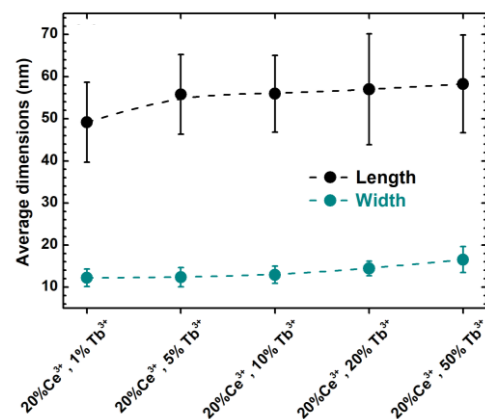
Table S9. Average dimensions of produced GdPO$_4$:20%Tb^{3+},x%Eu^{3+} samples.

Eu^{3+} conc.	Length, nm	Standard deviation, nm	Width, nm	Standard deviation, nm
1%	92	16	20	4
5%	71	8	38	5
10%	62	9	34	4
20%	55	9	28	5
50%	54	8	28	5
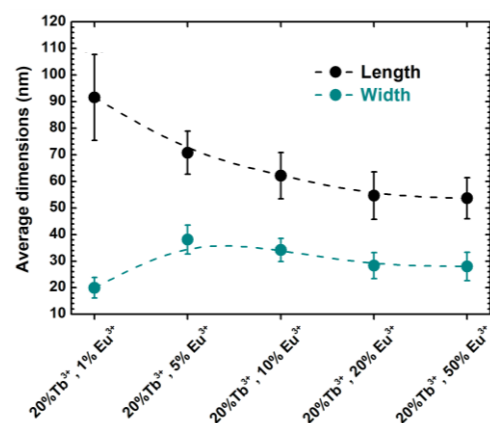
Table S10. Average dimensions of produced GdPO$_4$:20%Ce^{3+},x%Eu^{3+} samples.

Eu^{3+} conc.	Length, nm	Standard deviation, nm	Width, nm	Standard deviation, nm
1%	52	11	12	2
5%	53	10	13	2
10%	56	10	13	2
20%	51	12	12	2
50%	41	11	10	2
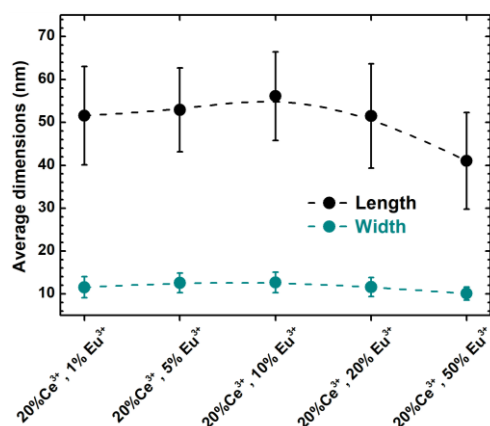
Table S11. Average dimensions of produced $GdPO_4$:20%Ce^{3+},20%Tb^{3+},x%Eu^{3+} samples.

Eu^{3+} conc.	Length, nm	Standard deviation, nm	Width, nm	Standard deviation, nm
1%	52	11	12	2
5%	53	11	11	2
10%	53	10	12	2
20%	53	11	11	2
50%	51	11	11	2
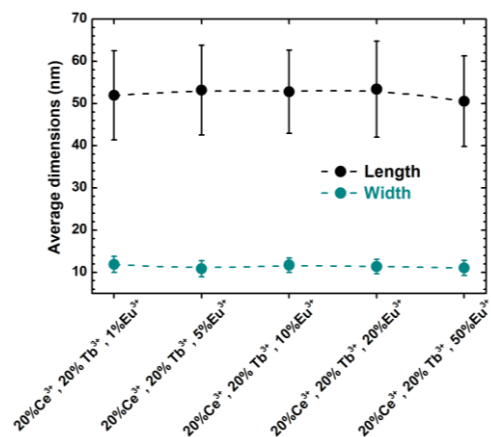
Table S12. Average dimensions of produced $GdPO_4$:15%Eu^{3+} samples.

Morphology of $GdPO_4$:15%Eu^{3+} NPs	Length, nm	Standard deviation, nm	Width, nm	Standard deviation, nm
Nanorods	73	10	15	2
Nanoprisms	94	13	57	6
Sub-microspheres	–	–	117	13

PL LIFETIME VALUES OF THE SYNTHESIZED PHOSPHORS

Table S13. PL lifetime values (λ_{ex} = 275 nm, λ_{em} = 350 nm) of GdPO$_4$:Ce^{3+} phosphors.

Ce^{3+}, %	τ_1, ns	Std. Dev.$_1$, ns	Rel$_1$, %	τ_2, ns	Std. Dev.$_2$, ns	Rel$_2$, %	τ_3, ns	Std. Dev.$_3$, ns	Rel$_3$, %	$\tau_{1/e}$, ns	Std. Dev., ns
5	3.37	0.02	47.09	17.31	0.14	33.11	450.65	11.94	19.80	**96.55**	**2.42**
10	3.11	0.02	43.80	15.82	0.13	31.46	483.71	11.23	24.74	**126.01**	**2.83**
20	2.86	0.02	47.66	13.99	0.14	30.01	378.94	8.08	22.33	**90.18**	**1.86**
25	2.66	0.02	47.52	13.32	0.12	31.98	335.55	6.80	20.50	**74.31**	**1.44**
50	1.83	0.02	49.72	8.37	0.09	42.41	87.73	2.24	7.87	**11.36**	**0.22**

Table S14. Temperature-dependent PL lifetime values (λ_{ex} = 275 nm, λ_{em} = 350 nm) of GdPO$_4$:20%Ce^{3+} phosphors.

T, K	τ_1, ns	Std. Dev.$_1$, ns	Rel$_1$, %	τ_2, ns	Std. Dev.$_2$, ns	Rel$_2$, %	τ_3, ns	Std. Dev.$_3$, ns	Rel$_3$, %	$\tau_{1/e}$, ns	Std. Dev., ns
77	0.15	0.01	30.39	4.16	0.1	32.09	16.13	0.25	37.52	**7.43**	**0.13**
100	0.12	0.01	28.31	4.32	0.08	35.36	18.03	0.23	36.33	**8.11**	**0.11**
150	0.14	0.01	32.83	4.59	0.08	38.23	21.07	0.33	28.94	**7.90**	**0.13**
200	0.11	0.03	31.77	3.97	0.07	38.06	18.66	0.31	30.17	**7.18**	**0.13**
250	0.16	0.01	38.87	5.05	0.07	35.23	19.78	0.56	25.9	**6.96**	**0.17**
300	0.11	0.03	47.99	3.22	0.07	33.83	18.8	0.49	18.17	**4.56**	**0.13**
350	0.09	0.02	41.32	2.87	0.06	39.96	21.91	0.65	18.72	**5.29**	**0.15**
400	0.18	0.04	60.48	1.43	0.09	34.5	19.77	0.28	5.02	**1.59**	**0.07**
450	0.19	0.01	68.83	3.25	0.13	28.41	18.13	0.43	2.76	**1.55**	**0.06**
500	0.12	0.01	71.14	2.17	0.06	22.36	9.15	0.51	6.51	**1.17**	**0.05**

Table S15. PL lifetime values (λ_{ex} = 340 nm, λ_{em} = 542 nm) of GdPO$_4$:Tb^{3+} phosphors.

Tb^{3+}, %	τ_1, ms	Std. Dev.$_1$, ms	Rel$_1$, %	τ_2, ms	Std. Dev.$_2$, ms	Rel$_2$, %	$\tau_{1/e}$, ms	Std. Dev., ms
1	2.04	0.02	40.24	5.59	0.03	59.76	**4.16**	**0.02**
5	2.25	0.02	45.51	4.99	0.03	54.49	**3.74**	**0.03**
10	2.07	0.03	33.91	4.01	0.03	66.09	**3.35**	**0.03**
20	1.39	0.05	12.16	2.96	0.01	87.84	**2.76**	**0.02**
50	0.58	0.01	32.43	1.20	0.01	67.57	**0.99**	**0.01**

Table S16. Temperature-dependent PL lifetime values (λ_{ex} = 340 nm, λ_{em} = 542 nm) of GdPO$_4$:20%Tb^{3+} phosphors.

T, K	τ_1, ms	Std. Dev.$_1$, ms	Rel$_1$, %	τ_2, ms	Std. Dev.$_2$, ms	Rel$_2$, %	$\tau_{1/e}$, ms	Std. Dev., ms
77	1.61	0.04	38.88	3.13	0.04	61.12	2.54	0.04
100	1.74	0.03	47.89	3.36	0.05	52.11	2.59	0.04
150	1.70	0.04	38.45	3.30	0.04	61.55	2.68	0.04
200	1.52	0.04	29.00	3.17	0.03	71.00	2.69	0.03
250	1.13	0.04	15.53	2.95	0.01	84.47	2.67	0.02
300	0.97	0.03	12.52	2.93	0.01	87.48	2.69	0.01
350	1.14	0.03	16.88	3.17	0.01	83.12	2.83	0.02
400	1.44	0.03	15.84	5.76	0.02	84.16	5.08	0.02
450	1.22	0.02	16.36	5.43	0.02	83.64	4.74	0.02
500	0.92	0.01	18.90	4.87	0.02	81.10	4.12	0.01

Table S17. PL lifetime values (λ_{ex} = 393 nm, λ_{em} = 587.5 nm) of GdPO$_4$:Eu^{3+} phosphors.

Eu^{3+}, %	τ_1, ms	Std. Dev.$_1$, ms	Rel$_1$, %	τ_2, ms	Std. Dev.$_2$, ms	Rel$_2$, %	$\tau_{1/e}$, ms	Std. Dev., ms
0.5	1.03	0.01	23.86	3.67	0.01	76.14	3.04	0.01
1	0.99	0.01	26.02	3.57	0.01	73.98	2.90	0.01
2.5	1.03	0.01	30.80	3.40	0.01	69.20	2.67	0.01
5	1.04	0.01	40.94	3.00	0.01	59.06	2.20	0.01
7.5	0.96	0.01	51.35	2.49	0.02	48.65	1.71	0.01
10	0.97	0.01	59.33	2.18	0.03	40.67	1.47	0.02
20	0.54	0.03	14.73	1.05	0.01	85.27	0.97	0.01
50	0.36	0.03	16.32	0.65	0.01	83.68	0.60	0.01

Table S18. Temperature-dependent PL lifetime values (λ_{ex} = 393 nm, λ_{em} = 587.5 nm) of GdPO$_4$:50%Eu^{3+} phosphors.

T, K	τ_1, ms	Std. Dev.$_1$, ms	Rel$_1$, %	τ_2, ms	Std. Dev.$_2$, ms	Rel$_2$, %	$\tau_{1/e}$, ms	Std. Dev., ms
77	0.48	0.02	9.69	0.91	0.01	90.31	0.87	0.01
100	0.46	0.02	10.13	0.87	0.01	89.87	0.83	0.01
150	0.40	0.02	11.79	0.79	0.01	88.21	0.74	0.01
200	0.31	0.01	9.04	0.71	0.01	90.96	0.67	0.01
250	0.33	0.01	12.33	0.67	0.01	87.67	0.63	0.01
300	0.33	0.01	16.07	0.64	0.01	83.93	0.59	0.01
350	0.27	0.01	11.80	0.60	0.01	88.20	0.56	0.01
400	0.28	0.01	25.50	0.59	0.01	74.50	0.51	0.01
450	0.24	0.01	27.76	0.48	0.01	72.24	0.41	0.01
500	0.14	0.01	27.82	0.30	0.01	72.18	0.26	0.01

Table S19. PL lifetime values (λ_{ex} = 275 nm, λ_{em} = 350 nm) of GdPO$_4$:20%Ce^{3+},x%Tb^{3+} phosphors.

Tb^{3+}, %	τ_1, ns	Std. Dev.$_1$, ns	Rel$_1$, %	τ_2, ns	Std. Dev.$_2$, ns	Rel$_2$, %	τ_3, ns	Std. Dev.$_3$, ns	Rel$_3$, %	$\tau_{1/e}$, ns	Std. Dev., ns
5	1.46	0.09	14.45	5.23	0.21	48.64	203.8	1.1	36.91	**77.98**	**0.52**
10	3.01	0.02	48.79	15.2	0.14	32.87	330.29	7.31	18.33	**67.01**	**1.40**
20	2.34	0.02	55.98	11.67	0.12	33.18	228.56	7.48	10.84	**29.96**	**0.86**
25	1.11	0.02	51.91	5.39	0.07	41.74	143.97	1.15	6.35	**11.97**	**0.11**
50	0.31	0.01	69.76	1.83	0.13	22.11	5.59	0.38	8.12	**1.07**	**0.07**

Table S20. Temperature-dependent PL lifetime values (λ_{ex} = 275 nm, λ_{em} = 350 nm) of GdPO$_4$:20%Ce^{3+},20%Tb^{3+} phosphor.

T, K	τ_1, ns	Std. Dev.$_1$, ns	Rel$_1$, %	τ_2, ns	Std. Dev.$_2$, ns	Rel$_2$, %	τ_3, ns	Std. Dev.$_3$, ns	Rel$_3$, %	$\tau_{1/e}$, ns	Std. Dev., ns
77	0.14	0.01	57.89	1.96	0.15	18.12	6.91	0.26	23.98	**2.09**	**0.10**
100	0.11	0.01	56.1	1.63	0.25	17.19	5.94	0.75	26.7	**1.93**	**0.25**
150	0.14	0.01	61.28	1.73	0.18	17.06	6.17	0.37	21.66	**1.72**	**0.12**
200	0.12	0.01	61.58	1.61	0.11	19.45	6.5	0.26	18.97	**1.62**	**0.08**
250	0.22	0.01	65.87	1.58	0.09	18.96	6.82	0.34	15.17	**1.48**	**0.08**
300	0.18	0.01	64.23	1.42	0.1	16.74	6.12	0.73	19.03	**1.52**	**0.16**
350	0.17	0.01	68.93	0.82	0.16	14.56	5.26	0.52	16.51	**1.10**	**0.12**
400	0.09	0.02	73.59	0.51	0.14	12.64	4.97	0.38	13.77	**0.82**	**0.08**
450	0.08	0.02	75.26	0.49	0.12	13.35	5.02	0.28	11.39	**0.70**	**0.06**
500	0.10	0.02	81.25	0.55	0.25	12.34	4.38	0.62	6.41	**0.43**	**0.09**

Table S21. PL lifetime values (λ_{ex} = 486 nm, λ_{em} = 542 nm) of GdPO$_4$:20%Tb^{3+},x%Eu^{3+} phosphors.

Eu^{3+}, %	τ_1, ms	Std. Dev.$_1$, ms	Rel$_1$, %	τ_2, ms	Std. Dev.$_2$, ms	Rel$_2$, %	τ_3, ms	Std. Dev.$_3$, ms	Rel$_3$, %	$\tau_{1/e}$, ms	Std. Dev., ms
0.5	0.29	0.03	2.26	1.39	0.04	48.95	2.48	0.04	64.72	**1.90**	**0.04**
1	0.35	0.02	9.25	1.15	0.02	73.47	2.46	0.08	48.79	**1.30**	**0.03**
2.5	0.29	0.01	18.9	0.87	0.01	64.68	2.54	0.04	17.28	**1.03**	**0.02**
5	0.27	0.01	20.92	0.94	0.01	53.96	3.27	0.03	16.42	**1.39**	**0.02**
7.5	0.26	0.01	28.57	0.86	0.02	48.11	3.08	0.04	25.12	**1.21**	**0.02**
10	0.23	0.00	29.51	0.76	0.02	45.1	2.96	0.03	23.32	**1.16**	**0.02**
20	0.16	0.00	38.61	0.60	0.01	41.03	2.60	0.03	25.39	**0.84**	**0.01**
50	0.13	0.00	27.45	0.87	0.02	37.08	2.12	0.08	20.36	**1.11**	**0.04**

Table S22. Temperature-dependent PL lifetime values (λ_{ex} = 486 nm, λ_{em} = 542 nm) of GdPO$_4$:20%Tb^{3+},10%Eu^{3+} phosphor.

T, K	τ_1, ms	Std. Dev.$_1$, ms	Rel$_1$, %	τ_2, ms	Std. Dev.$_2$, ms	Rel$_2$, %	τ_3, ms	Std. Dev.$_3$, ms	Rel$_3$, %	$\tau_{1/e}$, ms	Std. Dev., ms
77	0.20	0.01	14.47	0.81	0.02	56.28	2.39	0.04	29.25	1.19	0.02
100	0.22	0.01	18.09	0.83	0.02	55.30	2.55	0.05	26.61	1.18	0.03
150	0.01	0.00	36.72	0.38	0.00	35.31	1.77	0.01	27.97	0.63	0.00
200	0.05	0.00	9.97	0.44	0.01	56.47	1.95	0.02	33.55	0.91	0.01
250	0.01	0.00	47.65	0.31	0.00	31.52	1.65	0.02	20.83	0.45	0.00
300	0.17	0.01	25.70	0.60	0.03	44.90	2.32	0.07	29.41	1.00	0.03
350	0.13	0.01	21.63	0.48	0.02	45.85	2.10	0.05	32.52	0.93	0.03
400	0.13	0.00	26.94	0.49	0.02	41.67	2.19	0.06	31.39	0.93	0.03
450	0.06	0.00	13.26	0.34	0.01	42.93	2.04	0.05	43.81	1.05	0.03
500	0.01	0.00	79.21	0.21	0.00	10.54	1.82	0.03	10.25	0.22	0.00

Table S23. PL lifetime values (λ_{ex} = 275 nm, λ_{em} = 350 nm) of GdPO$_4$:20% Ce^{3+},x%Eu^{3+} phosphors.

Eu^{3+}, %	τ_1, ns	Std. Dev.$_{\cdot 1}$, ns	Rel$_1$, %	τ_2, ns	Std. Dev.$_{\cdot 2}$, ns	Rel$_2$, %	τ_3, ns	Std. Dev.$_{\cdot 3}$, ns	Rel$_3$, %	$\tau_{1/e}$, ns	Std. Dev., ns
0.5	1.57	0.06	18.52	5.79	0.13	47.12	22.01	0.45	34.36	**10.58**	**0.23**
1	1.81	0.03	31.54	7.29	0.11	47.01	30.93	0.51	21.45	**10.63**	**0.17**
2.5	1.43	0.02	49.49	6.83	0.08	39.77	35.28	0.62	10.74	**7.21**	**0.11**
5	0.59	0.01	47.94	2.86	0.06	36.48	12.66	0.22	15.59	**3.30**	**0.06**
7.5	0.12	0.01	48.39	1.18	0.04	34.73	5.74	0.12	16.88	**1.44**	**0.04**
10	0.15	0.03	61.34	0.86	0.09	25.92	3.37	0.27	12.74	**0.74**	**0.08**
20	0.06	0.02	80.24	0.77	0.12	13.97	4.82	1.93	5.80	**0.44**	**0.14**
50	0.05	0.01	83.87	0.96	0.14	10.83	3.59	0.45	5.29	**0.34**	**0.05**

Table S24. PL lifetime values (λ_{ex} = 275 nm, λ_{em} = 350 nm) of GdPO$_4$:20%Ce^{3+},20%Tb^{3+},x%Eu^{3+} phosphors.

Eu^{3+}, %	τ_1, ns	Std. Dev.$_{\cdot 1}$, ns	Rel$_1$, %	τ_2, ns	Std. Dev.$_{\cdot 2}$, ns	Rel$_2$, %	τ_3, ns	Std. Dev.$_{\cdot 3}$, ns	Rel$_3$, %	$\tau_{1/e}$, ns	Std. Dev., ns
0.5	0.67	0.02	43.66	3.18	0.04	46.04	14.17	0.28	10.31	**3.22**	**0.06**
1	0.79	0.02	51.53	3.35	0.06	40.42	14.93	0.36	8.05	**2.96**	**0.06**
2.5	0.5	0.02	55.39	2.4	0.05	35.51	9.29	0.26	9.1	**1.97**	**0.05**
5	0.19	0.02	57.92	1.34	0.04	31.87	5.51	0.12	10.21	**1.10**	**0.04**
7.5	0.14	0.02	70.09	1.18	0.05	22.07	4.44	0.13	7.84	**0.71**	**0.04**
10	0.08	0.02	74.78	1.19	0.05	20.12	4.51	0.2	5.1	**0.53**	**0.04**
20	0.03	0.01	85.42	1.34	0.09	12.49	4.2	0.66	2.1	**0.28**	**0.03**
50	0.03	0.01	83.27	1.29	0.1	11.94	4.25	0.33	4.79	**0.38**	**0.04**

Table S25. PL lifetime values (λ_{ex} = 393 nm, λ_{em} = 586 nm) of GdPO$_4$:15%Eu^{3+} phosphors.

Morphology of GdPO$_4$:15%Eu^{3+} NPs	τ_1, ms	Std. Dev.$_{\cdot 1}$, ms	Rel$_1$, %	τ_2, ms	Std. Dev.$_{\cdot 2}$, ms	Rel$_2$, %	$\tau_{1/e}$, ms	Std. Dev., ms
Nanorods	0.68	0.02	35.93	1.27	0.01	64.07	1.06	0.01
Nanoprisms	0.71	0.02	40.29	1.25	0.02	59.71	1.03	0.02
Sub-microspheres	0.81	0.01	51.32	1.38	0.02	48.68	1.09	0.02

Table S26. Tb^{3+} concentration dependent $Ce^{3+} \rightarrow Tb^{3+}$ ET efficiency values of $GdPO_4:20\%Ce^{3+},x\%Tb^{3+}$ samples.

Tb^{3+}, %	1	5	10	20	50
ET efficiency, %	4	18	63	85	99

Table S27. Temperature-dependent $Ce^{3+} \rightarrow Tb^{3+}$ ET efficiency values of $GdPO_4:20\%Ce^{3+},20\%Tb^{3+}$ samples.

Temperature, K	77	100	150	200	250	300	350	400	450	500
ET efficiency, %	72	76	78	77	79	67	79	49	55	63

Table S28. Eu^{3+} concentration dependent $Tb^{3+} \rightarrow Eu^{3+}$ ET efficiency values of $GdPO_4:20\%Tb^{3+},x\%Eu^{3+}$ samples.

Eu^{3+}, %	0.5	1	2.5	5	7.5	10	20	50
ET efficiency, %	31	53	62	50	56	58	70	60

Table S29. Temperature-dependent $Tb^{3+} \rightarrow Eu^{3+}$ ET efficiency values of $GdPO_4:20\%Tb^{3+},10\%Eu^{3+}$ samples.

Temperature, K	77	100	150	200	250	300	350	400	450	500
ET efficiency, %	56	55	76	66	84	63	67	81	78	95

Table S30. Eu^{3+} concentration dependent $Ce^{3+} \rightarrow Eu^{3+}$ ET efficiency values of $GdPO_4:20\%Ce^{3+},x\%Eu^{3+}$ samples.

Eu^{3+}, %	0.5	1	2.5	5	7.5	10	20	50
ET efficiency, %	87	87	91	96	98	99	99	99

Table S31. Eu^{3+} concentration dependent ET efficiency values of $GdPO_4$:20%Ce^{3+},20%Tb^{3+},x%Eu^{3+} samples.

Eu^{3+}, %	0.5	1	2.5	5	7.5	10	20	50
ET efficiency, %	96	96	98	99	99	99	99	99